www.elsevier.com/locate/jaerosci

In silico assessment of mouth-throat effects on regional deposition in the upper tracheobronchial airways

P.G. Koullapis, L. Nicolaou, S.C. Kassinos

PII: S0021-8502(17)30300-2
DOI: https://doi.org/10.1016/j.jaerosci.2017.12.001
Reference: AS5227

To appear in: *Journal of Aerosol Science*

Received date: 25 August 2017
Revised date: 16 November 2017
Accepted date: 4 December 2017

Cite this article as: P.G. Koullapis, L. Nicolaou and S.C. Kassinos, *In silico* assessment of mouth-throat effects on regional deposition in the upper tracheobronchial airways, *Journal of Aerosol Science,* https://doi.org/10.1016/j.jaerosci.2017.12.001

In silico assessment of mouth-throat effects on regional deposition in the upper tracheobronchial airways.

P.G. Koullapis[a], L. Nicolaou[b], S.C. Kassinos[a,*]

[a] *Computational Sciences Laboratory (UCY-CompSci), Department of Mechanical and Manufacturing Engineering, University of Cyprus, Kallipoleos Avenue 75, Nicosia 1678, Cyprus*
[b] *Department of Mechanical Engineering, Imperial College London, Exhibition Road, London SW7 2AZ, UK*

Abstract

Regional deposition of inhaled medicines is a valuable metric of effectiveness in drug delivery applications to the lung. *In silico* methods are now emerging as a valuable tool for the detailed description of localized deposition in the respiratory airways. In this context, there is a need to minimize the computational cost of high-fidelity numerical approaches. Motivated by this need, the present study is designed to assess the role of the extrathoracic airways in determining regional deposition in the upper bronchial airways. Three mouth-throat geometries, with significantly different geometric and filtering characteristics, are merged onto the same tracheobronchial tree that extends to generation 8, and Large Eddy Simulations are carried out at steady inhalation flowrates of 30 and 60 L/min. At both flowrates, large flow field differences in the extrathoracic airways across the three geometries largely die out below the main bifurcation. Importantly, localized deposition frac-

---

*Corresponding author
Email address: `kassinos@ucy.ac.cy` (S.C. Kassinos)

tions are found to remain practically identical for particles with aerodynamic diameters of up to $d_p = 4\mu m$ and $d_p = 2.5\mu m$ at 30 and $60\,L/min$, respectively. For larger particles, differences in the localized deposition fractions are shown to be mainly due to variations in the mouth-throat filtering rather than upstream flow effects or differences in the local flow field. Deposition efficiencies in the individual airway segments exhibit strong correlations across the three geometries, for all particle sizes. The results suggest that accurate predictions of regional deposition in the tracheobronchial airways can therefore be obtained if the particle size distribution that escapes filtering in the mouth-throat (ex-cast dose) of a particular patient is known or can be estimated. These findings open the prospect for significant reductions in the computational expense, especially in the context of *in silico* population studies, where the aerosol size distribution and precomputed flow field from standardized mouth-throat models could be used with large numbers of tracheobronchial trees available in chest-CT databases.

Keywords:
particle deposition, upper tracheobronchial airways, Large Eddy Simulations, regional deposition, Computational Fluid Dynamics, ex-cast aerosol size distribution

1. Introduction

Drug delivery via the pulmonary route is widely used for the treatment of pulmonary infections and respiratory diseases such as asthma, Chronic Obstructive Pulmonary Disease (COPD) and cystic fibrosis. More recently, the inhaled route has also emerged as a promising method for the systemic administration of drugs, due to the favorable absorption characteristics of the lungs (Smyth and Hickey, 2011).

The amount of drug that deposits in different regions of the respiratory tract is an important factor that affects the efficacy of inhaled drug delivery. Knowledge of the regional deposition within the lungs can assist with drug dosing decisions, and is valuable in assessing the effectiveness of drug targeting strategies and in optimizing patient maneuvering during inhalation. However, determining regional deposition accurately is not an easy task.

In vivo, deposition patterns can be determined using nuclear imaging techniques, such as 2D gamma scintigraphy, single photon emission computed tomography (SPECT), or positron emission tomography (PET), by the addition of a radiolabel to the aerosol formulation (Conway, 2012). These methods have the advantage of describing the real state, but remain limited by a number of challenges, such as insufficient spatial resolution and concerns from patient exposure to radiation.

In vitro, regional deposition in the tracheobronchial (TB) tree can be determined by using replicas of human airways derived from Computed Tomography (CT) scans, and because higher doses of radioactivity can be applied, they often provide better spatial resolution relative to *in vivo* methods. However, they are time-consuming and cannot easily be performed on a routine basis. As a result, the current industry standard is the use of pharmacopeial induction ports mounted on cascade impactors, which provides estimates of total lung deposition (Olson et al., 2013). However, when the bioavailability of the drug is less than 100%, the deposited lung dose is overpredicted due to mucociliary clearance of the dose fraction deposited in the TB region (Olsson and Backman, 2014). In this case, the efficacy of drug delivery depends, in part, on the site of deposition within the airways. Therefore, quantifying regional deposition is important in assessing and optimizing the systemic delivery of drugs with limited lung bioavailability, as well as in topical treatments requiring the targeting of specific lung sites.

In silico models can complement *in vivo*/*in vitro* tests and provide detailed information on regional deposition patterns. They can be used to perform repeated numerical experiments aiming to isolate the effect of a particular variable, something that is difficult to achieve *in vitro* or *in vivo*. A concise critical review of Computational Fluid Dynamics (CFD) techniques for *in silico* studies of the upper airways is given in Koullapis et al. (2017).

Due to the geometrical complexity and high Reynolds numbers, especially at flowrates that are relevant to drug delivery via Dry Powder Inhalers (DPIs), airflow in the upper airways usually transitions to turbulence (Tawhai and Lin, 2011). Three different methods can be applied to solve the turbulent flow: direct numerical simulations (DNS), Reynolds averaged Navier-Stokes (RANS) and large eddy simulations (LES). DNS resolves the turbulent fluctuations at all scales, providing the most accurate picture of the flow (Nicolaou and Zaki, 2013), but still remains exceedingly costly to perform on current computers. Presently, most CFD studies solve only for the averaged (or mean) flow using the RANS equations. A large reduction in computational cost is achieved in comparison to DNS, however accurate prediction of the laminar-turbulent-laminar flow transition that occurs in the TB airways is challenging for RANS (Kleinstreuer and Zhang, 2010). A more robust choice is the method of Large Eddy Simulations (LES), where only the smallest scales of motion are discarded and accounted for via a model. The computational expense of LES is considerably higher than that of RANS, but it retains significantly more elements of the underlying turbulence physics (Radhakrishnan and Kassinos, 2009; Koullapis et al., 2016).

With increasing gains in computing power, LES has become affordable for research purposes, but its application remains challenging for both population studies, where a large sample would need to be simulated, and for routine clinical use on a patient-specific basis. Therefore, there is a need to reduce the computational times required to predict regional deposition. Moreover, whereas CT-reconstruction of the imaged TB airways is straightforward and semi-automated in specialized imaging softwares (Miyawaki et al., 2016b), reconstruction of the extrathoracic airways is more challenging due to the complexity of the structures in this region. Therefore, *in silico* assessments of regional deposition in the TB region can be accelerated further if reconstruction of a patient's MT geometry is not required. In addition to this, a large amount of chest CT-scans, which typically exclude the extrathoracic airways (Miyawaki et al., 2017), are available and could potentially be used for population studies of lung deposition.

The pronounced effect of geometric variation on deposition in the extrathoracic airways is well documented in the literature (Grgic et al., 2004a; Heenan et al., 2004; Burnell et al., 2007; Nicolaou and Zaki, 2013). Grgic et al. (2004a) performed measurements in several realistic MT geometries at flowrates of 30 and 90 L/min for particle diameters of 3-6.5μm. They found that both total and regional deposition exhibit large inter-subject differences, as well as intra-subject variability to a lesser extent. Deposition was found to occur primarily via impaction, and the mouth area was identified as the largest obstacle for inhaled aerosols. An empirical Reynolds number correction, $Re^{0.37}$, was applied to the Stokes number (Grgic et al., 2004b), which reduced scatter in the reported deposition efficiencies, and provided better collapse of their data onto a single curve.

In a later study, Nicolaou and Zaki (2013) examined the flow in a subset of four MT geometries used by Grgic et al. (2004a). Adopting an immersed boundary method to simplify the task of grid generation for the realistic airway geometries (Nicolaou et al., 2015), the authors performed DNS of the flow and related the predicted flow to the variations in deposition observed in the *in vitro* measurements. It was found that geometric variation, even within the same subject, has a large impact on both the mean velocity profiles and the turbulence intensities. Their analysis revealed that the empirical correlation $StkRe^{0.37}$ arises due to the fact that deposition in the airways occurs via both impaction and turbulent diffusion. More recently, the authors proposed the use of an instantaneous Stokes number, based on the local properties of the flow field, for a more accurate representation of particle transport and deposition in the airways (Nicolaou and Zaki, 2016).

In an effort to identify key geometric parameters governing MT deposition, Burnell et al. (2007) investigated retention of drug aerosols inhaled from four delivery devices in 12 physical MT models *in vitro*. They found that deposition in the 12 models was dependent on the inhalation delivery system and that the most influential factor in MT deposition was the total volume. The airway geometries were ranked based on their retention efficiency and three models that represent high, median and low oropharyngeal filtration were identified. They suggested that these three models may reasonably cover the range of MT dimensions in the adult population and could therefore be used to indicate the expected range of MT deposition.

Besides the effect of geometric variability, previous studies have shown the importance of taking into account the laryngeal jet in order to accurately predict the airflow and aerosol deposition in the central airways. Lin et al. (2007) published the first DNS study in a subject-specific model of the upper airways with and without the MT region. They highlighted the role of the laryngeal jet in the production of turbulence downstream of the glottis constriction and concluded that subject-specific evaluations should include the extrathoracic airways. In a similar study, Xi et al. (2008) examined airflow and particle deposition in the upper TB airways in models with and without an approximate larynx using RANS. Significant differences were revealed between the two TB models in terms of flow patterns, aerosol dynamics, and wall deposition values.

In an LES study, Choi et al. (2009) investigated further the effect of truncation of the extrathoracic airways on the airflow in the trachea and downstream regions, in an effort to reduce imaging and computational costs. It was observed that the larger the truncation, the more inaccurate the flow fields. However, when the geometry was truncated at the midpharynx and a uniform velocity boundary condition was imposed, the predicted maximum mean velocity and rms fluctuations in the trachea and the distal bronchial airways were in fair agreement with the complete geometry. Working towards the same goal, Miyawaki et al. (2017) proposed an idealised laryngeal model that can be attached to the imaged central airways starting from the trachea.

It was found that by imposing isotropic turbulent conditions proximal to the glottis, the laryngeal model approximation could reproduce a realistic level of turbulence compared to the full geometry containing the patient's mouth-throat. In addition, it was concluded that if particle deposition in the central airways is of interest, inclusion of the extrathoracic region may not be necessary.

In the current study, an *in silico* assessment of MT effects on deposition in the central airways is carried out. Three extrathoracic airway geometries, with different geometric and deposition characteristics, are merged onto the same TB tree that extends to generation 8. LES simulations are performed at steady inhalation flowrates of 30 and 60 L/min, which are relevant to drug delivery applications. The objective of this investigation is to quantify the effect of geometric (and thus flow field) variations in the extrathoracic airways on regional aerosol deposition in the first few generations of the human TB tree. The critical question we address is whether standardized MT models can be used to predict regional deposition in the bronchial airways with acceptable accuracy. A positive answer to this question would result in three important advantages:

1. Imaging and reconstructing the patient's extrathoracic airways would not be required. This would accelerate *in silico* assessments, and would be beneficial for the patient as it reduces exposure to radiation.
2. Precomputed flow fields in these standard MT models could be adopted for predictions of deposition in the bronchial tree, which would result in significant computational savings.
3. It could provide a rational approach to using the large number of chest

CT-scans lacking MT data for *in silico* population studies.

The paper is organized as follows: Section 2 presents the airway geometries employed in this study, the numerical method adopted for the solution of the flow equations, and the particle-tracking scheme. Validation cases are also reported. In Section 3, results are presented for the airflow and particle deposition across the airway geometries at two flow rates, $Q = 30\,,60\,L/min$. Finally, in Section 4 we summarize the main findings of the current study and discuss limitations and future extensions.

2. Methods

2.1. Airway geometries

Three extrathoracic geometries, extending from a circular inlet at the mouth to the upper trachea, were merged onto the same model of the intrathoracic airways. The three MT models are shown in fig. 1.

[Figure 1 about here.]

The first geometry, R1, was developed by Lovelace Respiratory Research Institute. Details on the dimensions of the model are provided in Cheng et al. (1997). The anterior oral cavity was molded from an *in vivo* dental impression of a living Caucasian male at approximately 50% of full opening, and the remaining model was cast postmortem. The two other MT geometries, S1a and S2, were used in the *in vitro* deposition measurements of Grgic et al. (2004a) and in the DNS study of Nicolaou and Zaki (2013). These models were obtained using magnetic resonance imaging (MRI), as explained in detail by McRobbie et al. (2003). The main dimensions of the three MT models are listed in Table 1. The equivalent mean diameter was calculated assuming a circular cross-sectional area,

$$D_{mean} = 2\sqrt{\frac{V}{\pi L}}\,, \tag{1}$$

where V is the volume of the geometry and L is the sagittal length. The degree of area constriction at the glottis, which affects the characteristics of the laryngeal jet (Choi et al., 2009), is also reported in Table 1 ($A_{glottis}/A_{trachea}$).

[Table 1 about here.]

The considerable variations in the geometric characteristics of the three MT models result in notable differences in the airflow fields, which are discussed in the following section. In addition, their respective filtering efficiencies also show large deviations. This is reflected in figures 13(b) and 19(b), where the CFD-predicted deposition fractions for the three MT models are shown as a function of particle size at inhalation flowrates of 30 L/min and 60 L/min, respectively. Model R1 has the lowest deposition and S1a the highest. In all three cases, deposition increases with particle size. For the purpose of the present study, differences in the extrathoracic airways are desirable since we are seeking to quantify their effect on the regional deposition in the upper TB region. Thus, the three models (R1, S1a and S2) were chosen to provide a large degree of variability in the geometric characteristics, the flow field, and the filtering properties.

The TB geometry is shown in fig. 2. The model was obtained from a high-resolution CT of the lungs of an adult male free of pathological alterations, excised at autopsy and fixed in nearly end-inspiratory volume (Schmidt et al., 2004). Geometrical details can be found in Lizal et al. (2015). Segments 23-32 are outlets used for connecting the relatively small terminal branches into one larger outlet. The TB airway geometry together with the R1 MT model were used by Lizal et al. (2015) to measure regional aerosol deposition *in vitro* via PET. In section 2.3, we use these *in vitro* results for validation of our *in silico* predictions.

[Figure 2 about here.]

Finally, fig. 3 shows the three merged geometries used in our study. The MT geometries S1a and S2 were merged with the TB tree so that the location of the glottis constriction remained at the same height level as in geometry R1. In order to ensure a smooth geometric transition from the MT to the TB region, cubic spline interpolation was applied at multiple points along the circumferences of the MT outlet and the TB model inlet. The curves were then used to generate smooth surfaces that join the two domains. The merging procedure was carried out in Ansys ICEM CFD meshing software. Zoom-in locations in fig. 3(b) and (c) illustrate front and side views of the merging regions, in the upper and lower panels respectively.

[Figure 3 about here.]

2.2. Simulation Details

2.2.1. Continuous phase

Large Eddy Simulations (LES) are performed using the dynamic version of the Smagorinsky-Lilly subgrid scale model (Lilly, 1992) in order to examine the unsteady flow in the realistic airway geometries. Previous studies have shown that this model performs well in transitional flows in the human airways (Radhakrishnan and Kassinos, 2009; Koullapis et al., 2016). The airflow is described by the filtered set of incompressible Navier-Stokes equations,

$$
\begin{aligned}
\frac{\partial \bar{u}_j}{\partial x_j} &= 0 && (2)\\
\frac{\partial \bar{u}_i}{\partial t} + \bar{u}_j \frac{\partial \bar{u}_i}{\partial x_j} &= -\frac{1}{\rho}\frac{\partial \bar{p}}{\partial x_i} + \frac{\partial}{\partial x_j}\left[(\nu + \nu_{sgs})\frac{\partial \bar{u}_i}{\partial x_j}\right]. && (3)
\end{aligned}
$$

Here, $\bar{u}_i$, $\bar{p}$, $\rho = 1.2 kg/m^3$, $\nu = 1.7 \times 10^{-5} m^2/s$ and ν_{sgs} are the velocity component in the i-direction, the pressure, the density and kinematic viscosity of air, and the subgrid-scale (SGS) turbulent eddy viscosity, respectively. The overbar denotes resolved quantities.

The effect of the MT geometry on deposition in the central airways is examined for steady inhalation flowrates of 30 and 60 L/min. Table 2 summarizes the bulk velocity and Reynolds number at the mouth inlet and the trachea, which are given by,

$$U_b = \frac{Q}{A}, \qquad Re = \frac{U_b D}{\nu},$$

where the inlet and trachea diameters are used for the mouth inlet and the trachea, respectively.

[Table 2 about here.]

For the lower flowrate of 30 L/min, the Reynolds number at the inlet of models R1 and S2 is in the laminar regime and thus a parabolic velocity profile is imposed. For all other cases, the Reynolds number at the inlets is in the transitional to turbulent regime. In order to generate appropriate inlet velocity conditions, a mapped inlet (or recycling) boundary condition is used (Tabor et al., 2004). To apply this boundary condition, the pipe at the inlet is extended by a length equal to ten times its diameter. The pipe section is initially fed with an instantaneous turbulent velocity field generated in a separate pipe flow LES. During the simulation, the velocity field from the mid-plane of the pipe domain is mapped to the inlet boundary. Scaling of the velocities is applied to enforce the specified bulk flow rate. In this manner, turbulent flow is sustained in the extended pipe section, and a turbulent velocity profile enters the mouth inlet.

The volumetric flowrates at the 10 terminal outlets are prescribed based on the values measured *in vitro* (Lizal et al., 2015). These outlet conditions result in high asymmetry in the ventilation of the two lungs: the left lung receives 29% of the inhaled air whereas the right lung receives 71%. A no-slip velocity condition is imposed on the airway walls and atmospheric pressure is set at the inlet boundary.

The governing equations (eqn. 2 and 3) are discretized using a finite volume method and solved using OpenFOAM, an open-source CFD code. The scheme is second-order accurate in both space and time. To ensure numerical stability the time steps used are 5 and 2.5 $\times 10^{-6}$ s for the cases of 30 and 60 L/min, respectively. The mesh densities used in the three cases are determined based on a preliminary mesh sensitivity study carried out in the S1a MT model. The final generated meshes consist of approximately 50 million computational cells. Further details on the mesh convergence study are provided in Section 2.3.

2.2.2. Particle phase

Spherical, rigid and non-rotating particles are introduced at the mouth inlet. Using a Lagrangian approach, the motion of each particle is individually computed by solving Newton's equations to determine the particle velocity, $\vec{u}_p$, and position, $\vec{x}_p$,

$$m_p \frac{d\vec{u}_p}{dt} = \vec{F}_D + \vec{F}_G + \vec{F}_B, \qquad \frac{d\vec{x}_p}{dt} = \vec{u}_p \,. \tag{4}$$

Here m_p is the particle mass, and $\vec{F}_D$, $\vec{F}_G = m_p\vec{g}$, and $\vec{F}_B$ are the drag, gravity, and Brownian forces, respectively. The gravitational acceleration vector, $\vec{g}$, points in the downward vertical direction.
The drag force acting on the spherical particles is given by,

$$\vec{F}_D = \frac{m_p}{\tau_p}(\vec{\bar{u}} - \vec{u}_p)\,, \tag{5}$$

where $\vec{\bar{u}}$ is the filtered fluid velocity interpolated at the position of the particle and τ_p is the particle response time, defined as:

$$\tau_p = \frac{\rho_p d_p^2 C_c}{18\mu_f C_D \frac{Re_p}{24}}\,, \tag{6}$$

with ρ_p=914 kg/m^3 being the particle density, d_p the particle diameter, $\mu_f = 2.04 \times 10^{-5} kg/ms$ the dynamic fluid viscosity and $Re_p = d_p|\vec{\bar{u}} - \vec{u}_p|/\nu_f$ the particle Reynolds number. C_c is the Cunningham correction factor, which accounts for slip at the particle surface due to non-continuum effects. It is defined as $C_c = 1 + \frac{2\lambda}{d_p}\left[1.257 + 0.4\exp(-0.55d_p/\lambda)\right]$, where λ=0.070μm is the mean free path of air. The drag coefficient, C_D, is based on the correlation proposed by Schiller and Naumann (1935):

$$C_D = \begin{cases} \frac{24}{Re_p}(1 + 0.15 Re_p^{0.687}) & \text{if } Re_p \leq 1000 \\ 0.44 & \text{if } Re_p > 1000\,. \end{cases} \tag{7}$$

The Brownian force is important for submicron particles and causes diffusion due to collisions with the air molecules (Finlay, 2001). The expression for the amplitude of its ith component is based on the correlation proposed by Li and Ahmadi (1992),

$$F_{B,i} = \zeta_i \sqrt{\frac{1}{\tilde{D}} \frac{2k_B^2 T^2}{\Delta t}}\,, \tag{8}$$

where ζ_i is a zero mean variant from a Gaussian probability density function, T=310K is the absolute temperature, $\tilde{D} = (k_B T C_c)/(3\pi\mu_f d_p)$ is the Brownian diffusion coefficient, $k_B = 1.3806488 \times 10^{-23}$ m^2 kg /s$^2 K$ is the Boltzmann constant and Δt is the time step used for integration of the particle equations.

At each time step, the flow equations are solved first in order to obtain the filtered fluid velocity field needed for the calculation of the drag force. Then, eqn. 4 is integrated with an implicit Euler scheme. The particle-tracking algorithm developed by Macpherson et al. (2009) is adopted. At every time step 10 particles for each size are released from random positions at the mouth inlet. Particles are released over a time period equal to a flow-through in the trachea, and the total number of injected particles is 100,000 for each particle size. The initial velocity of the particles is set to match the air velocity at the inlet. A particle is considered deposited if the distance from its centre to the airway wall is equal or less than the particle radius. One-way coupling is considered, assuming dilute particle suspensions.

2.3. Validation

2.3.1. Airflow

In order to determine the required mesh density for our simulations, a set of preliminary LES in MT model S1a were performed on different mesh sizes, and the results were compared to DNS data (Nicolaou and Zaki, 2013). Geometry S1a was selected among the three MT models as the most challenging case due to the higher inlet Reynolds number, which results in turbulent inlet conditions even at the lower flowrate of 30 L/min. Since the flow relaminarizes in the downstream regions, the mesh convergence study was limited to the MT region. Turbulent velocity conditions were imposed at the inlet using the mapped inlet boundary condition. At the outlet, a convective outflow condition was applied, in accordance to the DNS simulations of Nicolaou and Zaki (2013).

Four meshes with increasing densities were generated, designated as Meshes 1 to 4. The near-wall region was resolved with prismatic elements, while the core of the domain was meshed with tetrahedral elements. Cross-sectional views of the four meshes near the inlet of S1a are shown in fig. 4. Table 3 reports grid characteristics, such as the initial cell height (Δr_{min}), the number of prism layers near the walls, the average expansion ratio of the prism layers (λ), the total number of computational cells, the average cell volume ($V_{cell,avg.}$) and the average and maximum $y+$ values. In upper airway applications, turbulence is usually most active in the shear layers formed between high and low speed regions, such as the laryngeal jet (Tawhai and Lin, 2011). Thus, use of a strict $y^+ = 1$ condition for the near wall mesh is not essential. Based on this observation, the average cell volume of the generated meshes was approximately halved in every grid refinement. To further assess the mesh resolution near the walls, the number of prism layers was doubled and the spacing of the first computing node was reduced to one third in Mesh 4 compared to Mesh 3.

[Table 3 about here.]

[Figure 4 about here.]

Fig. 5 displays the contours of mean velocity magnitude in the central sagittal plane and at various cross-sections of MT S1a. Results obtained with the four different meshes are shown alongside the DNS data obtained using an immersed boundary method (Nicolaou et al., 2015). Fig. 6 shows 2D profiles of the mean velocity magnitude at the lines of intersection between cross-sections A1-A2 to E1-E2 and the central sagittal plane. The mean velocity contours and 2D profiles indicate small differences among the four meshes. The LES and DNS results are in good agreement overall, which suggests adequate resolution for this flow configuration. Some differences are found in the low-speed regions at cross-section C1-C2, which are likely due to numerical or subgrid turbulence modelling aspects.

[Figure 5 about here.]

[Figure 6 about here.]

Based on the findings presented above, meshes with densities similar to Mesh 2 were generated for the three MT-TB models, and LES simulations were carried out at inlet flowrates of 30 and 60 L/min.

2.3.2. Particle deposition

For validation purposes, deposition in geometry R1 was compared to the *in vitro* measurements by Lizal et al. (2015). Fig. 7 displays the deposition fractions at the individual geometry segments numbered in fig. 2, for particles of size 4.3μm at flowrates of 15 and 60 L/min. The error bars attached to the *in vitro* results at $Q = 60\,L/min$ correspond to the estimated experimental uncertainties as reported by the authors (Lizal et al., 2015). Numerical and experimental results are shown to be in reasonable agreement. Possible reasons for the observed discrepancies include experimental uncertainties at the inlet related to the velocity profile and the particle distribution. The *in vitro* inlet conditions might deviate from the velocity profiles and uniform particle distribution assumed in the CFD simulations due to the effect of the devices located upstream of the mouth in the experimental apparatus (Lizal et al., 2015). Similar levels of deviation between numerical and *in vitro* deposition results were reported by Koullapis et al. (2017), who applied six different LES and RANS solvers with different particle-tracking schemes to geometry R1.

In order to assess the degree of uncertainties as compared with other existing measurement data, we have plotted our CFD-predicted deposition efficiencies in the distal branches along with *in vitro* results from Lizal et al. (2015), Zhou and Cheng (2005) and Chan and Lippmann (1980). Fig. 8 displays deposition efficiencies versus the Stokes number (Stk), which is calculated using the diameter and bulk velocity of the parent airway in a particular bifurcation. As can be seen in the deposition plot, our results fall within the scatter of the experimental data.

[Figure 7 about here.]

[Figure 8 about here.]

3. Results and Discussion

We begin by examining the flow and aerosol deposition across the three geometries at the lower inhalation flow rate, $Q = 30L/min$. The mean and turbulent flow characteristics in the extra- and intra-thoracic airways are presented first, followed by the results for regional deposition. The validity of the findings is then assessed at a higher inhalation flow rate, $Q = 60L/min$, in order to provide a conclusive picture of MT effects on the flow and regional deposition in the TB airways.

3.1. Lower inhalation rate, $Q = 30\,L/min$

3.1.1. Airflow

Figures 9 and 10 show contours of the mean velocity magnitude and turbulent kinetic energy, $k = \frac{1}{2}\,\overline{u_i'u_i'}$ (u_i' are the fluctuating velocities), in the MT region and the trachea across the three geometries. Fig. 9(a) also displays isosurfaces of the mean velocity that outline the laryngeal jet. The mean velocity and turbulent kinetic energy are normalized by the bulk velocity in the trachea. Large qualitative differences in the flow characteristics can be observed in the oral cavities, pharyngeal and laryngeal regions of the three models. In the oral cavities of R1 and S2, lower velocities are observed, due to the larger cross-sectional areas compared to S1a. Moreover, the recirculation regions at the top and bottom walls of the oral passage are larger in these two geometries. Differences can also be identified in the turbulent kinetic energy levels. The airflow entering the mouth of model S1a is in the transitional regime. As a result, higher values of k are recorded near the inlet of S1a compared to the other two geometries, where the inflow is laminar. Low velocities and levels of turbulent kinetic energy persist in the pharynx and larynx of R1. In S1a, the flow accelerates in the narrow larynx, and high turbulent kinetic energy levels appear at the height of the epiglottis, which are attributed to the formation of the separated shear layer. In S2, the flow accelerates at the entrance of the pharynx as a result of the large reduction in cross-sectional area, and the maximum kinetic energy is observed in this region. In all three geometries, recirculation zones are found near the anterior wall at the height (R1, S2) and downstream (S1a) of the epiglottis, due to the airway curvature. These flow characteristics are consistent with the observations of Nicolaou and Zaki (2013), where a more detailed description of the airflow in geometries S1a and S2 is provided.

An important flow feature in the extrathoracic airways, which determines the mean and fluctuating behaviors of the flow downstream, is the laryngeal jet (Choi et al., 2009). The characteristics of the laryngeal jet are notably different in the three cases and are largely affected by the degree of constriction at the glottis (see Table 1). Geometry R1 has a mild glottal constriction ($< 30\%$ reduction in area at the glottis), resulting in a low-speed jet that is too weak to induce significant mixing with the ambient air, as indicated by the low turbulent kinetic energy levels in the trachea (fig. 10(b)). On the other hand, the higher degree of glottal constriction in S1a and S2 results in much stronger turbulent fluctuations that are convected down to the trachea. In S1a, the narrower glottal passage, in conjunction with the forward inclination of the trachea, shifts the jet core towards the anterior wall of the upper trachea (velocity isosurfaces and stations A-C for S1a in fig. 9(a) and (b)) and leads to the formation of a large recirculation region near the rear wall. In S2, the laryngeal jet expands over a shorter length and a less pronounced recirculation zone develops due to the vertical orientation of the trachea below the glottis.

As we move to the mid-height of the trachea (station C), the flow has time to develop and differences in the mean velocity fields start to diminish notably, although variations are still evident in the turbulent kinetic energy levels. Further downstream (station D), differences in the mean flow and turbulence characteristics across geometries are further reduced and only small discrepancies remain, due to the effects of the upstream flow.

[Figure 9 about here.]

[Figure 10 about here.]

Contours of the normalized mean velocity magnitude in the main bronchi, and in the smaller airways of generations 3 and 4, are shown in fig. 11. A notable feature of the flowfield is the pronounced asymmetry at the main bifurcation, marked by a much larger recirculation zone near the outer wall of the left main bronchus (fig. 11(a)). The asymmetry in the flow reflects that of the airways; the left main bronchus branches off the carina at an angle of 60^o, significantly larger than the 48^o branching angle of the right bronchus. The recirculation regions are qualitatively similar across the three geometries, and only minor differences are observed at the main bifurcation and in the left main bronchus (fig. 11(a)). Slightly larger variations exist in the right main bronchus, which can be attributed to the higher ventilation of the right lung. Further down the TB tree, we continue to observe a similar trend. Variations in the flow are more prominent in the right lung, mainly in the recirculation regions, as shown in fig. 11(c). Overall however, despite significant differences in the extrathoracic flow dynamics, the mean velocity in the TB tree remains qualitatively similar across the three geometries.

The corresponding results for the turbulent field in the TB tree are shown in fig. 12. Higher levels of turbulent kinetic energy are observed in the central bifurcation and the right main bronchus of models S1a and S2 (fig. 12(a)) compared to geometry R1. These differences can be attributed to the stronger turbulent intensities arising in the upstream regions of S1a and S2 that are then convected into the TB tree. Minor differences in turbulent kinetic energy levels, between S1a and S2 on one hand and R1 on the other, persist in the distal regions of the left and right lungs, as shown in figs. 12(b) and 12(c), respectively. It should be noted that turbulent kinetic energy levels in the bronchial airways are approximately an order of magnitude smaller than the values recorded in the extrathoracic regions, and thus the transport of particles is not expected to be affected significantly by these low intensity turbulent fluctuations.

In summary, the effect of geometric variation on the mean and turbulent flow characteristics in the extrathoracic region was found to be significant across the three geometries. This is to be expected, since the three models were chosen so as to provide a large degree of variability. The differences in the flow fields, however, settled down to relatively minor discrepancies in the bronchial tree. In the next section, we examine the regional particle deposition, in order to determine the impact of upstream flow effects and differences in the local flow field on TB deposition.

[Figure 11 about here.]

[Figure 12 about here.]

3.1.2. Particle deposition

Fig. 13 shows the deposition fractions as a function of particle size at $30\,L/min$ in (a) the overall geometry, (b) the mouth-throat region, and (c) the tracheobronchial tree. In addition, Fig. 13(c) displays particle sizes in terms of the Stokes number based on the mean diameter and bulk velocity in the trachea,

$$Stk_{trachea} = \frac{\rho_p d_p^2 U_{trachea}}{18 \mu_f D_{trachea}}\,, \tag{9}$$

where $U_{trachea}$ is given in Table 2 and $D_{trachea} = 1.63\,cm$.

Deposition results in the overall geometry follow a similar trend to MT deposition, with model S1a having the highest values and R1 the lowest. However, differences in the overall deposition across the three geometries are significantly smaller than those noted for MT deposition. This is due to reverse filtering effects occurring in the TB and MT regions that tend to partially compensate for each other. While in the MT region the highest and lowest deposition fractions correspond to models S1a and R1, respectively, in the TB region these trends are reversed, as shown in fig. 13(c). It is also worth noting that in the TB region, deposition appears to be appreciable at seemingly very small Stokes numbers ($Stk < 5 \times 10^{-2}$). This is attributed to the fact that the reported Stokes numbers are calculated based on the mean diameter and bulk velocity in the trachea and thus do not reflect the local properties of the geometry and the flowfield (Nicolaou and Zaki, 2016). In geometry S1a, deposition of the $10\mu m$ particles in the TB region is lower than for the smaller particles of 6 and $8\mu m$, due to the significant filtering that occurs upstream in the extrathoracic airways. It is important to note that for particles smaller than $4\mu m$ ($Stk_{trachea} < 5.94 \times 10^{-3}$), TB deposition is unaffected by the MT model. Even for $6\mu m$ particles ($Stk_{trachea} = 1.34 \times 10^{-2}$), the maximum variation in TB deposition is less than 4% and, reduces below 3% if differences in deposition in the trachea (segment 2) are excluded. Therefore, these results suggest that for particle sizes typically used in drug delivery applications, i.e. 1-5 microns, localized deposition in the central airways is largely unaffected by the MT geometry.

Deposition within the TB tree can be examined in further detail by determining the deposition fractions in individual airway segments, as shown in fig. 14 for various particle sizes at $30\,L/min$. Beyond the trachea, and for particles smaller than $6\mu m$, similar deposition fractions are observed across the three geometries, even at the localized level. Essentially, for particles smaller than $4\mu m$, differences are negligible in the vast majority of segments within the TB region. For larger particles with diameters above $8\mu m$, variability in TB regional deposition across the three geometries becomes more significant. This variation arises due to the large differences in the MT filtering, which are as high as 70% for $10\mu m$ particles between geometries S1a and R1 (fig. 13(b)).

The conclusions made herein are based on results at $30\,L/min$. However, many inhaler devices, such as DPIs, typically operate at higher inhalation flowrates (Wong et al., 2012). Therefore, in the following section, we assess the validity of these findings at a higher flowrate of 60 L/min.

[Figure 13 about here.]

[Figure 14 about here.]

3.2. Higher inhalation rate, $Q = 60\,L/min$

3.2.1. Airflow

Figures 15 and 16 show contours of the normalized mean velocity magnitude and turbulent kinetic energy in the MT region and the trachea across the three geometries at a flowrate of 60 L/min. Fig. 15(a) also displays isosurfaces of normalized mean velocity that outline the laryngeal jet. The mean flow features remain similar to those noted for the lower flowrate. Nevertheless, small reductions in the magnitudes of the normalized mean velocities are evident at this higher flowrate. These lower velocities result from the increased turbulent mixing that occurs as the flowrate, and hence the Reynolds number, doubles. Turbulent kinetic energy levels in the MT and the trachea also exhibit strong resemblance to those observed at the lower flowrate, with the local maxima appearing at the same locations. As in the lower flowrate case, the effect of geometric variation is clearly evident in the MT region. However, at the exit to the trachea (D1-D2), the flow is qualitatively similar across all three geometries despite the higher flowrate and increased turbulence levels.

[Figure 15 about here.]

[Figure 16 about here.]

As we move deeper into the TB tree, first into the main bronchi and then into bronchial generations 3 and 4, the mean velocity fields are again found to remain similar across the three cases, as shown in fig. 17. The same holds for the turbulent kinetic energy levels in the TB region, shown in fig. 18. In conclusion, despite significant differences in the extrathoracic flow features, the mean and turbulent fields in the TB tree remain qualitatively similar across the three geometries even at a flowrate of $60\,L/min$.

[Figure 17 about here.]

[Figure 18 about here.]

3.2.2. Particle deposition

Fig. 19 shows the deposition fractions versus particle size at $60\,L/min$ in (a) the overall geometry, (b) the mouth-throat region, and (c) the tracheobronchial tree. In fig. 19(c), the Stokes number based on tracheal parameters is also displayed. At this flowrate, greater differences are observed in the overall deposition of the smaller particles among the three models (fig. 19(a)). MT deposition is again significantly different across the three geometries, and notably at this flowrate, a larger variation is observed for the intermediate particle sizes. In S1a, the largest particles are almost entirely filtered out in the MT (fig. 19(b)). For particles larger than $2.5\mu m$, deposition in the TB region is inversely related to the MT filtering: model R1 has the highest TB deposition, and S1a the lowest. For particles smaller than $2.5\mu m$ ($Stk_{trachea} < 4.64 \times 10^{-3}$), TB deposition is unaffected by the MT, whereas for $4\mu m$ particles ($Stk_{trachea} = 1.19 \times 10^{-2}$) the maximum variation in TB deposition is 7.5%.

[Figure 19 about here.]

Fig. 20 shows the deposition fractions in the individual airway segments for various particle sizes. For particles smaller than $2.5\mu m$ and downstream of the first bifurcation (segment 3), segmental deposition fractions are in good agreement across the three geometries. At $d_p = 4\mu m$, slight differences in localized deposition are observed. For larger particle sizes, the differences become non-negligible in most of the segments.

In order to assess whether the observed differences in localized deposition in the TB tree are partly due to local flowfield variations or entirely due to the differential filtering that occurs in the MT region, we examine the segmental deposition efficiencies, defined as the ratio of the number of particles depositing in a particular segment to the number of particles entering that segment. Fig. 21 shows the segmental deposition efficiencies for various particle sizes in the three models. The results show that localized filtering in the TB tree is practically unchanged among the three models for all particle sizes. Pairwise deposition efficiency scatter plots for the various particle sizes are shown in fig. 22. In order to quantify the degree of similarity across the three geometries, pairwise correlation coefficients, r, are also reported in fig. 22. A good collapse of the deposition efficiency values on the $y = x$ line is evident, and the correlation coefficients, which in all but one case ($1\mu m$, R1 vs S2, $r = 0.9816$) are above 0.99, confirm a strong linear correlation. These results indicate that the minor differences observed in the local TB flow field are largely inconsequential as far as deposition is concerned, and that the variation in regional deposition fractions results from the differences in MT filtering.

3.2.3. Interpretation of results

The findings in this section provide useful insight on the suitability of standardized MT models for accurate predictions of regional deposition in the upper TB region. For particles with $Stk_{trachea} < 5.94 \times 10^{-2}$ ($d_p < 4\mu m$) at $Q = 30\, L/min$ and $Stk_{trachea} < 4.64 \times 10^{-2}$ ($d_p < 2.5\mu m$) at $Q = 60\, L/min$, localized deposition fractions in the TB tree remain practically unchanged independent of the MT geometry employed. By adopting the precomputed flow field from a standard MT model, simulations could therefore be restricted to the tracheobronchial tree resulting in significant computational savings. For larger particles however, TB deposition, as expressed in terms of deposition fractions, depends on the MT filtering. Therefore, in order to obtain accurate localized deposition estimates, a standardized MT model with similar filtering as the patient's MT should be selected. The question then becomes how to identify the standard model with similar filtering properties; the answer depends on the underlying objective. For example, one scenario is that of population studies aimed at identifying functional/structural parameters of the intrathoracic airways that determine regional TB deposition for various classes of patients. In this context, one could envisage using a small number of standardized MT geometries, selected so as to be representative of the expected variability in target patient populations. The aerosol size distribution that escapes MT filtering (ex-cast dose) and the precomputed flow field in these particular MT models could then be adopted, which would significantly minimize the time and cost required to compute regional deposition in the central airways. This would be of significant advantage in the context of population studies where large numbers of simulations have to be carried out in order to have an adequate statistical sample. A different scenario is that of patient-specific simulations. Here, the primary motivation is to spare the patient the need to image the extrathoracic airways and to minimize diagnosis time. In this context, further work is needed to identify key parameters that could be used to match the patient to a specific MT model. For example, Burnell et al. (2007) conducted an *in vitro* study across a number of MT geometries, in order to determine the key geometric characteristics governing mouth-throat deposition. Of 51 dimensional variables investigated, the single most influential factor was found to be the total volume of the extrathoracic airways. While not conclusive, such studies point to the possibility that a combination of structural and/or functional parameters (such as the patient's inhalation profile) could eventually be shown to provide a reliable means of classifying the patient's extrathoracic airways. Clearly, further work is needed in this direction in the form of combined *in vitro* and *in silico* studies, a goal that we are currently pursuing.

[Figure 20 about here.]

[Figure 21 about here.]

[Figure 22 about here.]

4. Conclusions

The objective of the current study was to quantify the effect of geometric variation in the mouth and throat on regional deposition in the first generations of a realistic TB tree. Three extrathoracic airways with different geometric and deposition characteristics were merged onto the same TB geometry, and the airflow and particle transport were simulated using LES under steady inhalation conditions at 30 and 60 L/min. The large flowfield differences observed in the extrathoracic airways and the trachea were found to largely vanish by the first bifurcation, and the mean flow features and turbulent kinetic energy levels in the TB region remained similar, regardless of the inhalation flowrate and the degree of glottal constriction. Localized deposition in the TB tree was practically unaffected by the MT filtering for particles smaller than $4\mu m$ ($Stk_{trachea} = 5.94 \times 10^{-3}$) at 30 L/min, and $2.5\mu m$ ($Stk_{trachea} = 4.64 \times 10^{-3}$) at 60 L/min. The variability in the deposition fractions at larger particle sizes was shown to be due to variation in the MT filtering across geometries, rather than differences in the local flow field. These findings suggest that accurate predictions of regional deposition in the TB airways can therefore be obtained using standardized MT models with similar filtering characteristics as the patient's extrathoracic airways. This approach would circumvent the need to image and reconstruct the extrathoracic airways, reducing patient exposure to radiation and accelerating *in silico* studies. Furthermore, by adopting the ex-cast dose and precomputed flow field from standardized MT models, significant computational savings can be achieved as simulations can be restricted to the TB region, without the need to include the extrathoracic airways.

In the work presented herein, we have merged three MT geometries with significantly different airflow characteristics as well as filtering efficiencies to a single TB tree. One would need to repeat this study with more geometries before attempting to generalize observations, nevertheless the prospect is promising. If the current results are found to be repeatable with different combinations of airway geometries, large-scale *in silico* studies of regional deposition in a large sample of TB tree geometries could be performed using a small set of representative ex-cast particle distributions that cover the desired cross-sections of patient populations. The large number of chest CT-scans that are available on medical databases, which typically exclude the extrathoracic airways, could therefore be utilized in population studies aimed at identifying the key factors that influence regional deposition patterns.

We note that in the present study we have adopted steady inspiratory flow rates, whereas patient-specific or inhaler-dependent inhalation waveforms are transient. Transient flow simulations would be required in order to assess whether the present findings are also valid under these inhalation conditions. Tian et al. (2011) numerically investigated the effect of transient vs. steady-state conditions and found that transient inhalation influences the deposition of particles in the MT and upper TB airways through the third generation, where the Womersley number is greater than 1. On the other hand, transient conditions were shown to have little influence on deposition in the TB regions located distally to the fourth generation, and a steady-state approximation accurately captured deposition. Deposition in the upper airways during the exhalation phase is considered to be minor compared to deposition upon inhalation (Finlay, 2001). For this reason, the majority of *in vitro* and *in silico* deposition studies in the upper airways consider only the inhalation phase (Grgic et al., 2004a; Lizal et al., 2015; Lambert et al., 2011). In addition to the flowrate profile, the velocity profiles at the mouth inlet were assumed to be parabolic or turbulent in the present study. In actual drug delivery applications through an inhaler, however, the inlet velocity profile could deviate from these conditions due to airflow structures convected from the device. The effect of inlet velocity profile on aerosol deposition in the upper airways was examined by Koullapis et al. (2016). Although the authors found that imposed conditions at the mouth inlet did indeed affect aerosol filtering in the oral cavity, differences in the flow field dissipated by the time the flow reached the mid-trachea. Therefore, while one might anticipate a weak effect of inlet conditions on localized deposition fractions in the TB tree, we expect the deposition efficiencies to remain fairly insensitive, and the conclusions of the present study to hold for different inlet conditions as well.

In our study the walls of the airway models were assumed rigid. In reality, however, lungs deform and thus, airway diameter and length vary during breathing. In a recent study, Miyawaki et al. (2016a) examined the effect of rigid vs deforming airways on particle transport and deposition in a subject-specific airway model of the central airways. A difference of 22% on average, depending on the generation number, was observed between the rigid and deforming models. Furthermore, the cumulative average deposition fraction in the rigid model was consistently smaller and the relative difference between the two models reached 13% in generation 4. In our study, since the same TB geometry is used in the three cases considered, the degree of uncertainty in deposition results due to airway deformation is expected to be similar in all cases.

Finally, we also note that for certain DPIs, flow rates as high as 90 L/min are relevant (Islam and Cleary, 2012). Extrapolating from the conclusions of the present work, at this high inhalation rate, one would expect smaller particle sizes to be affected by the differences in the MT filtering. Nevertheless, the expectation is that the deposition efficiencies would remain largely unaffected. Therefore, one of the main outcomes of this work would remain valid: ex-cast particle distributions (adjusted for flowrate and patient class) could be used to compute regional deposition in the proximal TB tree for *in silico* population studies or routine clinical use on a patient-specific basis.

Acknowledgements

The present study was funded by the European Union 7th framework program HEXACOMM FP7/2007-2013 under grant agreement N^o 315760. In addition, the authors would like to acknowledge the financial support provided by COST-European Cooperation in Science and Technology, to the COST Action MP1404: Simulation and pharmaceutical technologies for advanced patient-tailored inhaled medicines (SimInhale). Dr. Frantisek Lizal at Brno University is gratefully acknowledged for sharing with us the realistic human airway tree geometry and the *in vitro* deposition data.

References

Burnell, P. K. P., Asking, L., Borgstrom, L., Nichols, S. C., Olsson, B., Prime, D., Shrubb, I., 2007. Studies of the human oropharyngeal airspaces using magnetic resonance imaging IV - the oropharyngeal retention effect for four inhalation delivery systems. Journal of Aerosol Medicine 20 (3), 269–281.

Chan, T., Lippmann, M., 1980. Experimental measurements and empirical modelling of the regional deposition of inhaled particles in humans. American Industrial Hygiene Association Journal 41 (6), 399–409.

Cheng, K. H., Cheng, Y. S., Yeh, H. C., 1997. Measurements of airway dimensions and calculation of mass transfer characteristics of the human oral passage. Biomechanical Engineering 119, 476–482.

Choi, J., Tawhai, M., Hoffman, E., Lin, C.-L., 2009. On intra- and intersubject variabilities of airflow in the human lungs. Phys. Fluids 21 (101901).

Conway, J., 2012. Lung imaging - two dimensional gamma scintigraphy, SPECT, CT and PET. Advanced Drug Delivery Reviews 64 (4), 357–368.

Finlay, W. H., 2001. The Mechanics of Inhaled Pharmaceutical Aerosols. Academic Press, New York.

Grgic, B., Finlay, W. H., Burnell, P. K. P., Heenan, A. F., 2004a. In vitro intersubject and intrasubject deposition measurements in realistic mouth–throat geometries. Journal of Aerosol Science 35 (8), 1025–1040.

Grgic, B., Finlay, W. H., Heenan, A. F., 2004b. Regional aerosol deposition and ow measurements in an idealized mouth and throat. Journal of Aerosol Science 35, 21–32.

Heenan, A., Finlay, W., Grgic, B., Pollard, A., Burnell, P., 2004. An investigation of the relationship between the flow field and regional deposition in realistic extra-thoracic airways. Journal of Aerosol Science 35, 1013–1023.

Islam, N., Cleary, M. J., 2012. Developing an efficient and reliable dry powder inhaler for pulmonary drug delivery - a review for multidisciplinary researchers. Medical Engineering and Physics 34 (Islama), 409–427.

Kleinstreuer, C., Zhang, Z., 2010. Airflow and particle transport in the human respiratory system. Annual Review of Fluid Mechanics 42, 301–334.

Koullapis, P., Kassinos, S. C., Muela, J., Perez-Segarra, C., Rigola, J., Lehmkuhl, O., Cui, Y., Sommerfeld, M., Elcner, J., Jicha, M., Saveljic, I., Filipovic, N., Lizal, F., Nicolaou, L., 2017. Regional aerosol deposition in the human airways: The siminhale benchmark case and a critical assessment of in silico methods. European Journal of Pharmaceutical Sciences.
URL http://www.sciencedirect.com/science/article/pii/S0928098717304992

Koullapis, P. G., Kassinos, S., Bivolarova, M. P., Melikov, A. K., 2016. Particle deposition in a realistic geometry of the human conducting airways: Effects of inlet velocity profile, inhalation flowrate and electrostatic charge. Journal of Biomechanics 49, 2201–2212.

Lambert, A., O'Shaughnessy, P., Tawhai, M., Hoffman, E., Lin, C.-L., 2011. Regional deposition of particles in an imaged-based airway model: Large eddy simulation and left-right lung ventilation asymetry. Aerosol Science and Technology 45, 11–25.

Li, A., Ahmadi, G., 1992. Dispersion and deposition of spherical particles from point sources in a turbulent channel flow. Aerosol Science and Technology 16, 209–226.

Lilly, D. K., 1992. A proposed modification of the Germano subgrid-scale closure method. Physics of Fluids A 4 (3), 633–635.

Lin, C.-L., Tawhai, M., Mclennan, G., Hoffman, E., 2007. Characteristics of the turbulent laryngeal jet and its effect on airflow in the human intra-thoracic airways. Respiratory Physiology and Neurobiology 157, 295–309.

Lizal, F., Belka, M., Adam, J., Jedelsky, J., Jicha, M., 2015. A method for in vitro regional aerosol deposition measurement in a model of the human tracheobronchial tree by the positron emission tomography. Proceedings IMechanical E Part H, Engineering in Medicine 229 (10), 750–757.

Macpherson, G. B., Nordin, N., Weller, G., 2009. Particle tracking in unstructured, arbitrary polyhedral meshes for use in CFD and molecular dynamics. Communications in Numerical Methods in Engineering 25 (3), 263–273.

McRobbie, D., Pritchard, S., Quest, R., 2003. Studies of the human oropharyngeal airspaces using magnetic resonance imaging. I. Validation of a three-dimensional MRI method for producing ex vivo virtual and physical casts of the oropharyngeal airways during inspiration. Journal of Aerosol Medicineournal of Aerosol Medicine 16, 401–415.

Miyawaki, S., Hoffman, E. A., Lin, C.-L., 10 2016a. Effect of static vs. dynamic imaging on particle transport in CT-based numerical models of human central airways. Journal of Aerosol Science 100, 129–139.
URL http://www.ncbi.nlm.nih.gov/pmc/articles/PMC5224794/

Miyawaki, S., Hoffman, E. A., Lin, C.-L., 2017. Numerical simulations of aerosol delivery to the human lung with an idealized laryngeal model, image-based airway model, and automatic meshing algorithm. Computers & Fluids 148, 1–9.
URL http://www.sciencedirect.com/science/article/pii/S0045793017300531

Miyawaki, S., Tawhai, M. H., Hoffman, E. A., Wenzel, S. E., Lin, C.-L., 2016b. Automatic construction of subject-specific human airway geometry including trifurcations based on a CT-segmented airway skeleton and surface. Biomechanics and Modeling in Mechanobiology, 1–14.

Nicolaou, L., Jung, S. Y., Zaki, T. A., 2015. A robust direct-forcing immersed boundary method with enhanced stability for moving body problems in curvilinear coordinates. Computers and Fluids 119, 101–114.

Nicolaou, L., Zaki, T. A., 2013. Direct numerical simulations of flow in realistic mouth–throat geometries. Journal of Aerosol Science 57, 71–87.

Nicolaou, L., Zaki, T. A., 2016. Characterization of aerosol Stokes number in 90^o bends and idealized extrathoracic airways. Journal of Aerosol Science 102, 105–127.

Olson, D. E., Borgstrom, L., H., L., Svensson, M., 2013. Validation of a general in vitro approach for prediction of total lung deposition in healthy adults for pharmaceutical inhalation products. Journal of Aerosol Medicine and Pulmonary Drug Delivery 26 (0), 1–115.

Olsson, B., Backman, P., 2014. Mouth-throat models for realistic in vitro testing - a proposal for debate. Respiratory Drug Delivery 1, 287–294.

Radhakrishnan, H., Kassinos, S., 2009. CFD modeling of turbulent flow and particle deposition in human lungs. 31st Annual International Conference of the IEEE EMBS, Mineapolis, Minnesota, USA, 2867–2870.

Schiller, L., Naumann, Z., 1935. Ver. Deutsch Ing.

Schmidt, A., Zidowitz, S., Kriete, A., 2004. A digital reference model of the human bronchial tree. Comput Med Imaging Graph 28, 203–211.

Smyth, H. D. C., Hickey, A. J., 2011. Controlled Pulmonary Drug Delivery, Advances in Delivery Science and Technology Series. Springer, New York.

Tabor, G. R., Baba-Ahmadi, M. H., de Villiers, E., Weller, H. G., 2004. Construction of inlet conditions for LES of turbulent channel flow. European Congress on Computational Methods in Applied Sciences and Engineering (ECCOMAS).

Tawhai, M., Lin, C.-L., 2011. Airway gas flow. Comprehensive Physiology 1, 1135–1157.

Tian, G., Longest, P. W., Su, G., Walenga, R. L., Hindle, M., 2011. Development of a stochastic individual path (SIP) model for predicting the tracheobronchial deposition of pharmaceutical aerosols: effects of transient inhalation and sampling the airways. Journal of Aerosol Science 42, 781–99.

Wong, W., Fletcher, D. F., Traini, D., Chan, H.-K., Young, P. M., 2012. The use of computational approaches in inhaler development. Advanced Drug Delivery Reviews 64 (4), 312 – 322.
URL http://www.sciencedirect.com/science/article/pii/S0169409X11002730

Xi, J., Longest, P. W., Martonen, T. B., 2008. Effects of the laryngeal jet on nano- and microparticle transport and deposition in an approximate model of the upper tracheobronchial airways. Journal of Applied Physiology 104, 1761–1777.

Zhou, Y., Cheng, Y.-S., 2005. Particle deposition in a cast of human tracheobronchial airways. Aerosol Science and Technology 39 (6), 492–500.

List of Figures

(a) (b) (c)

Figure 1: Mouth-throat geometries adopted in the study: (a) R1, (b) S1a and (c) S2.

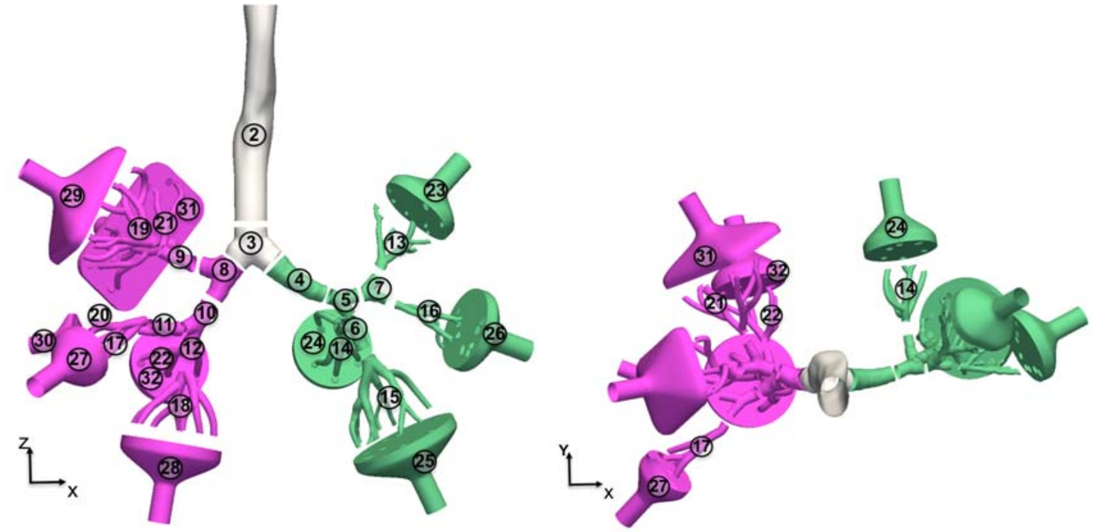

(a) (b)

Figure 2: Front (a) and upper (b) views of the tracheobronchial geometry used in the simulations. The numbering of the various segments is also shown. Segments in the left and right lung are colored in green and purple, respectively.

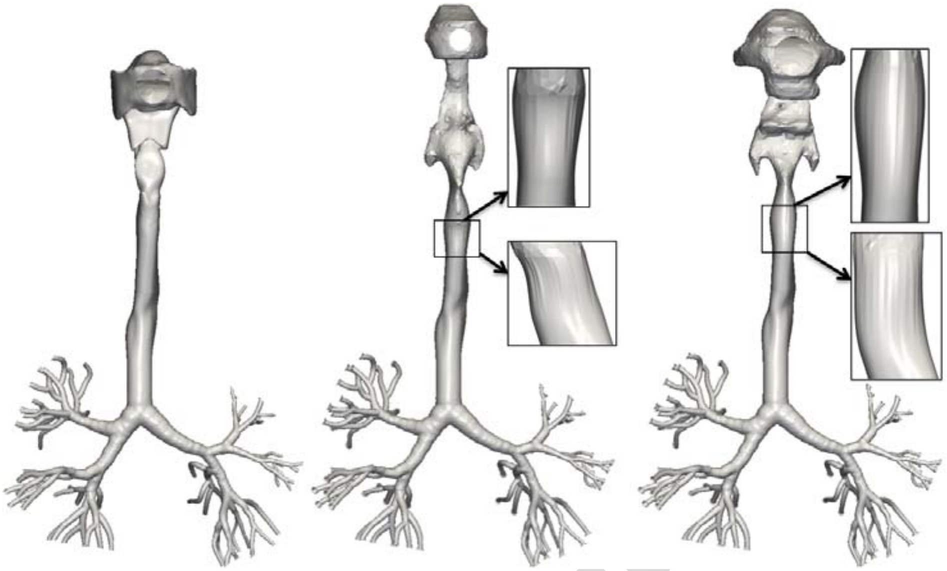

(a) (b) (c)

Figure 3: Final merged geometries corresponding to (a) R1, (b) S1a and (c) S2.

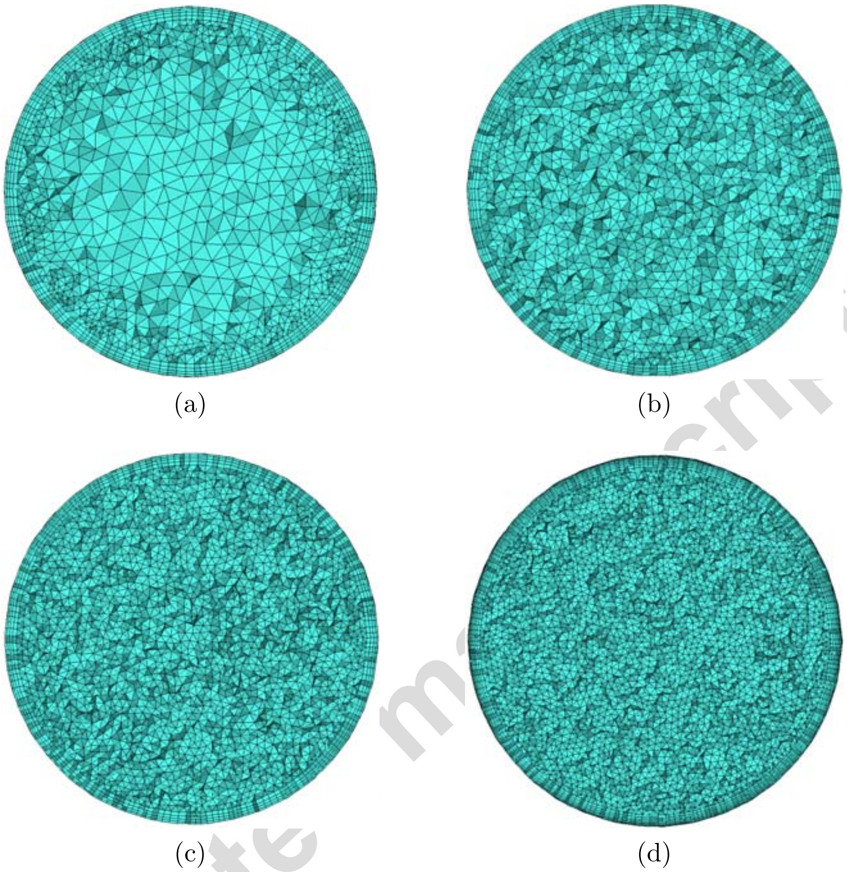
(a) (b) (c) (d)

Figure 4: Cross-sectional views of the four meshes near the inlet of geometry S1a: (a) Mesh 1 (7 million cells), (b) Mesh 2 (12 million cells), (c) Mesh 3 (24 million cells), (d) Mesh 4 (42 million cells).

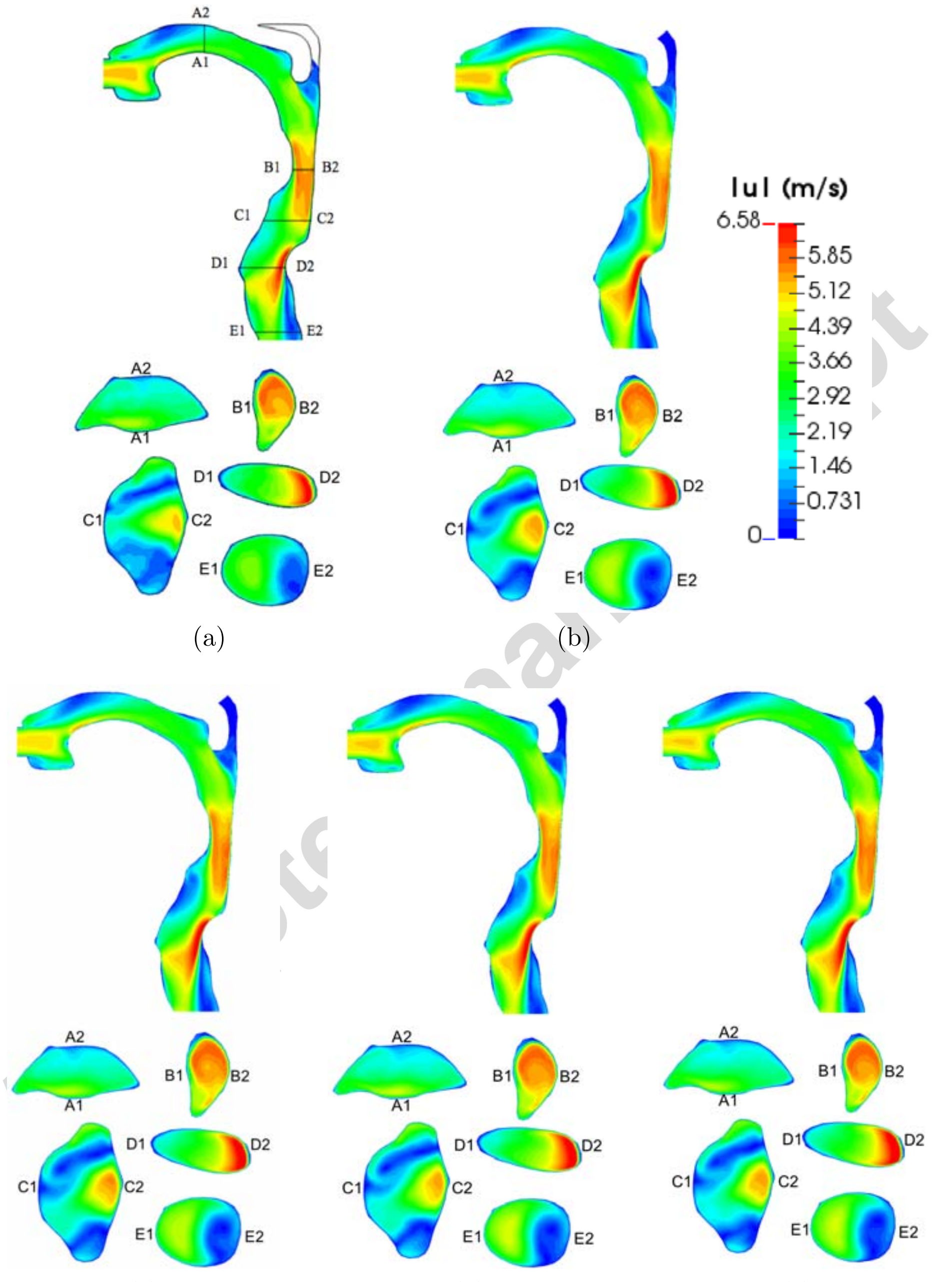

(a) (b)

(c) (d) (e)

Figure 5: Contours of mean velocity magnitude in the central sagittal plane and at various cross-sections of MT S1a: (a) DNS, (b) LES - Mesh 1, (c) LES - Mesh 2, (d) LES - Mesh 3, (e) LES - Mesh 4.

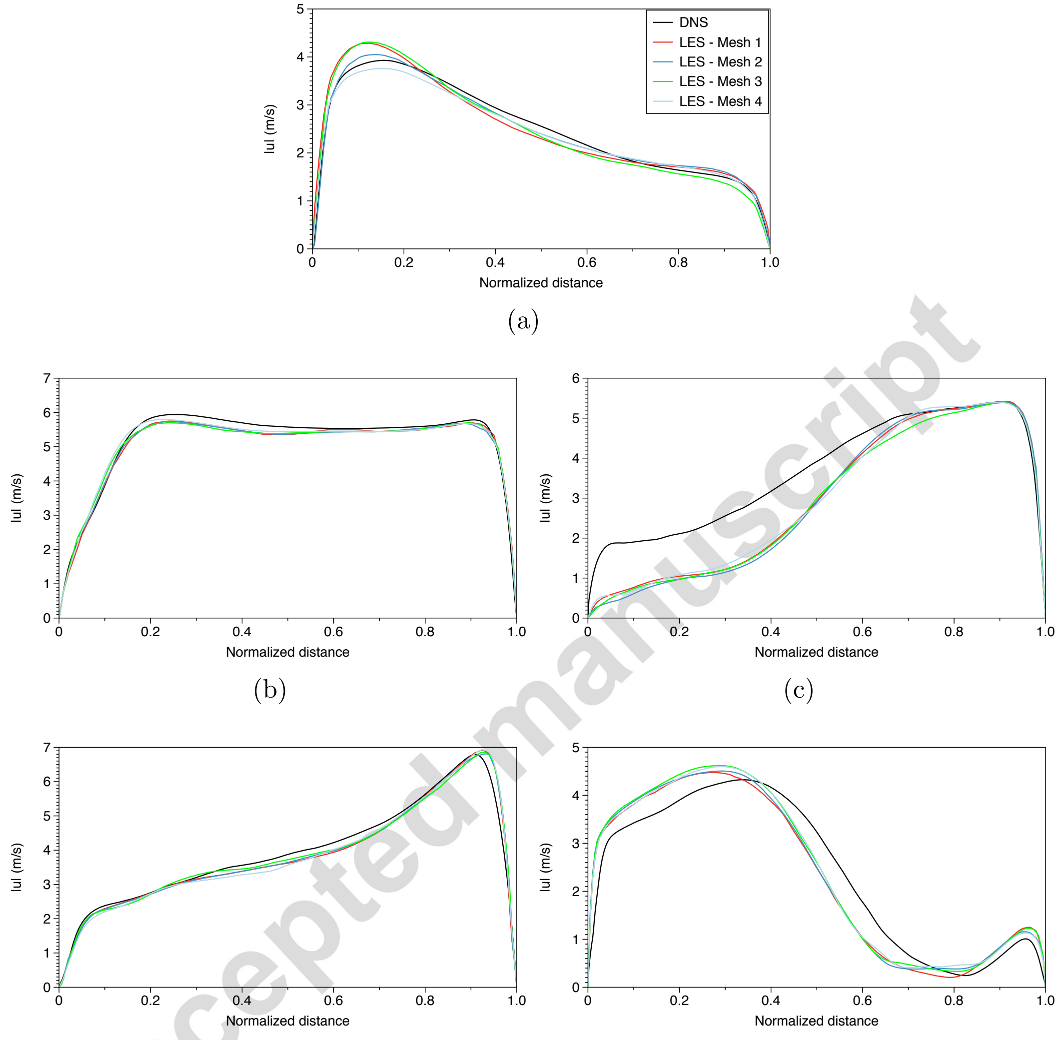

(a)

(b)

(c)

(d)

(e)

Figure 6: Profiles of mean velocity magnitude at the lines of intersection between cross-sections A1-A2 to E1-E2 and the central sagittal plane. (a) A1-A2 (b) B1-B2 (c) C1-C2, (d) D1-D2, (e) E1-E2.

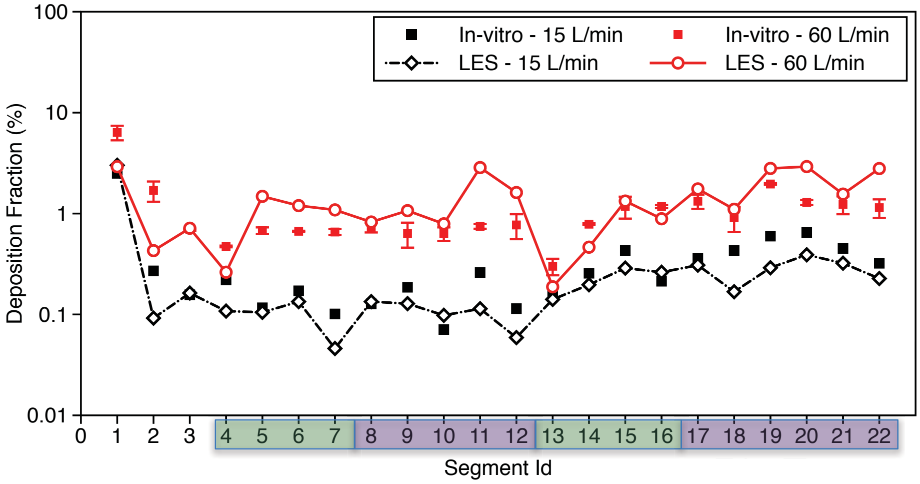

Figure 7: Deposition fractions per segment in geometry R1 for particles of size $4.3\mu m$ at inlet flowrates of 15 and $60\,L/min$. The numbering of the segments is shown in fig. 2. The green and purple coloring denotes segments in the left and right lung, respectively. Segment 1 corresponds to the MT region.

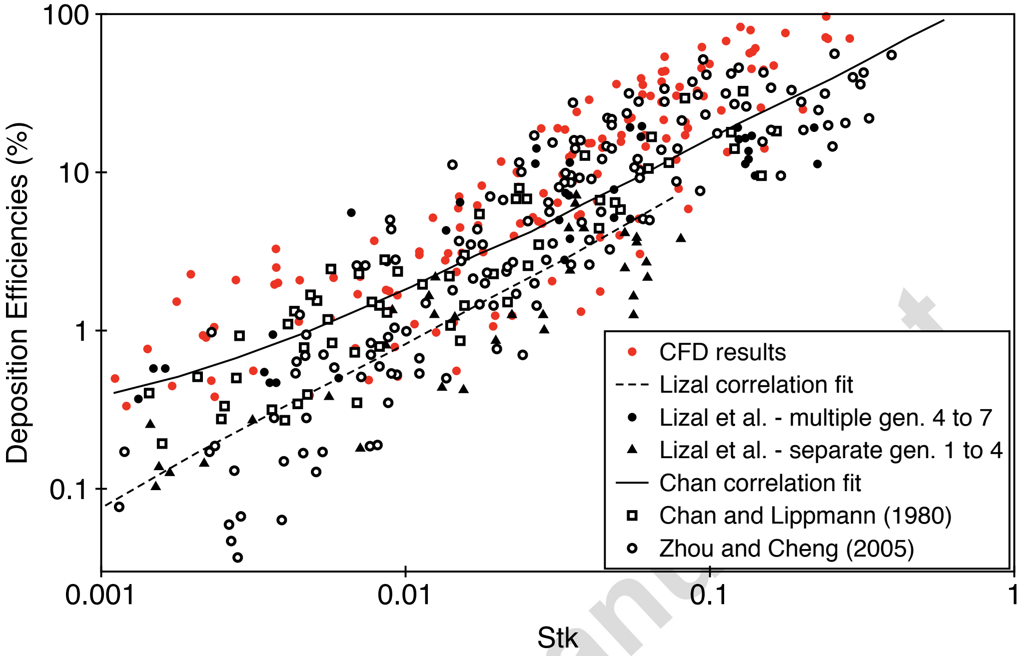

Figure 8: Comparison of the CFD-predicted deposition efficiencies with previously published experimental data (symbols) and correlation fits (lines).

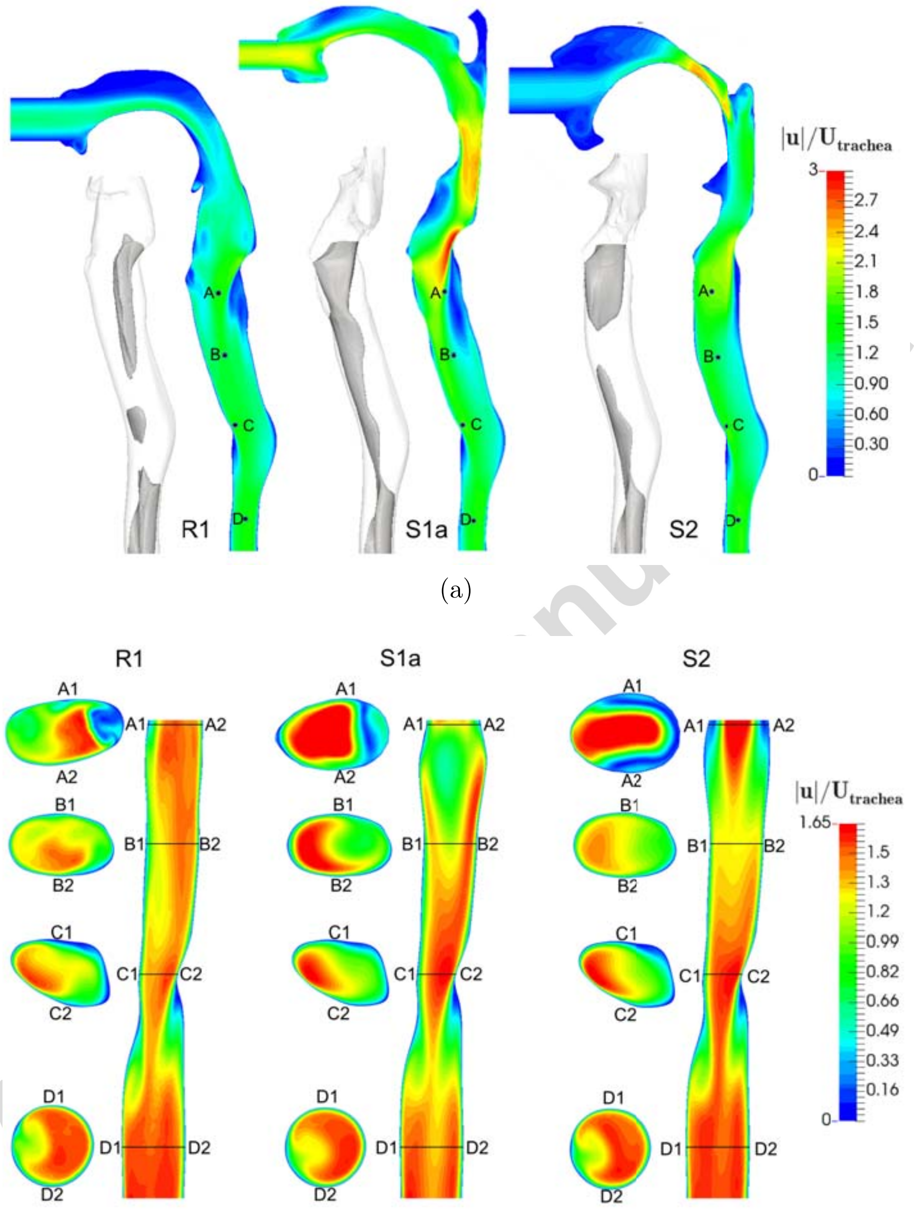

(a)

(b)

Figure 9: Contours of normalized mean velocity magnitude in (a) the mouth-throat region (side view), and (b) the trachea (top and front views) at $Q = 30\, L/min$. In (a) isosurfaces of $|u|/U_{trachea} = 1.45$ are shown.

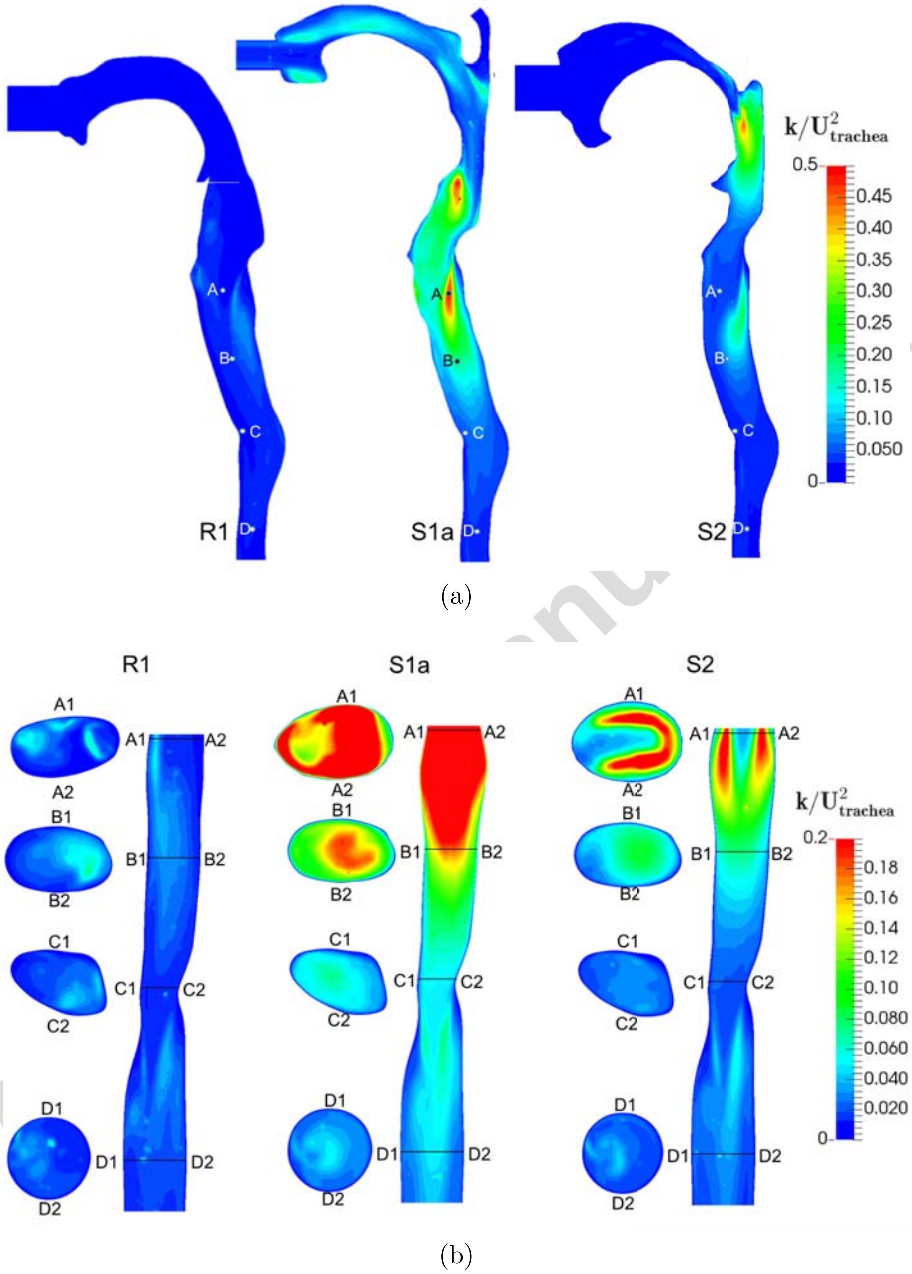

(a)

(b)

Figure 10: Contours of normalized turbulent kinetic energy in (a) the mouth-throat region (side view), and (b) the trachea (top and front views) at $Q = 30\,L/min$.

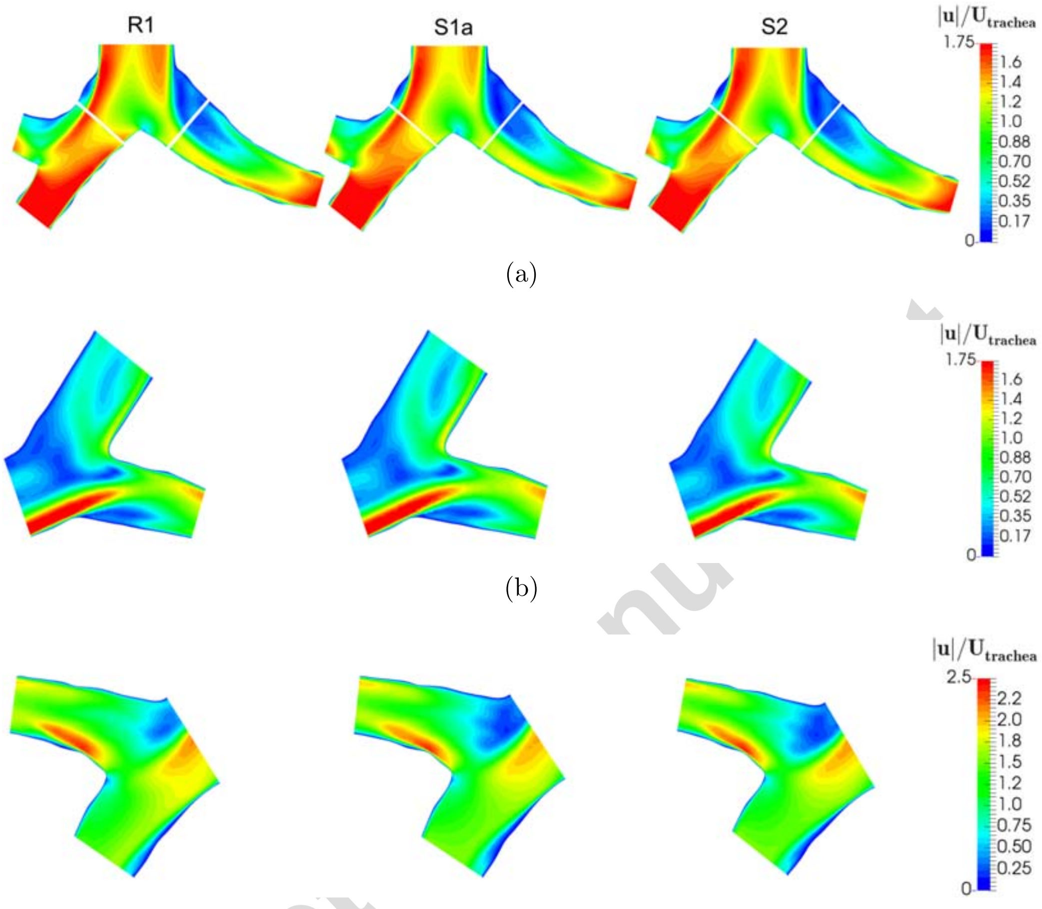

(a)

(b)

(c)

Figure 11: Contours of normalized mean velocity magnitude in the tracheobronchial tree at $Q = 30\,L/min$: (a) first bifurcation and main bronchi; (b) third to fourth generation bifurcation in the left lung; and (c) third to fourth generation bifurcation in the right lung.

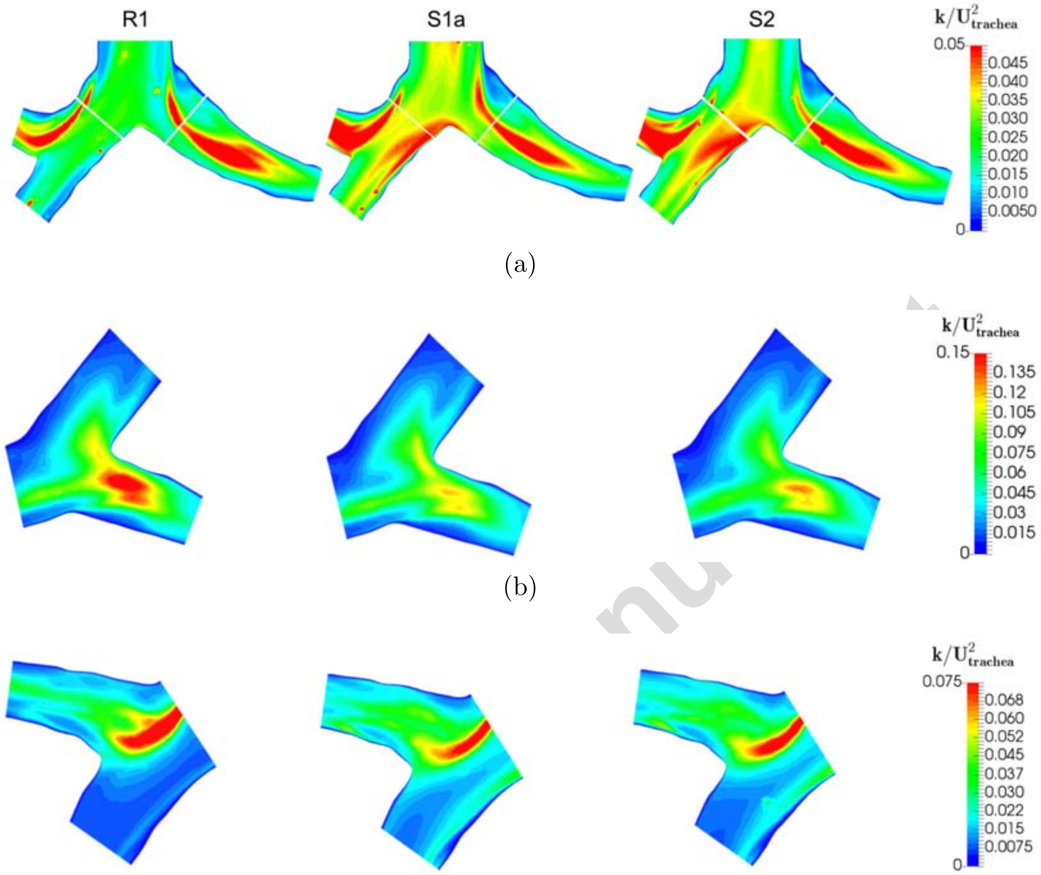

(a)

(b)

(c)

Figure 12: Contours of normalized turbulent kinetic energy in the tracheobronchial tree at $Q = 30\,L/min$: (a) first bifurcation and main bronchi; (b) third to fourth generation bifurcation in the left lung; and (c) third to fourth generation bifurcation in the right lung.

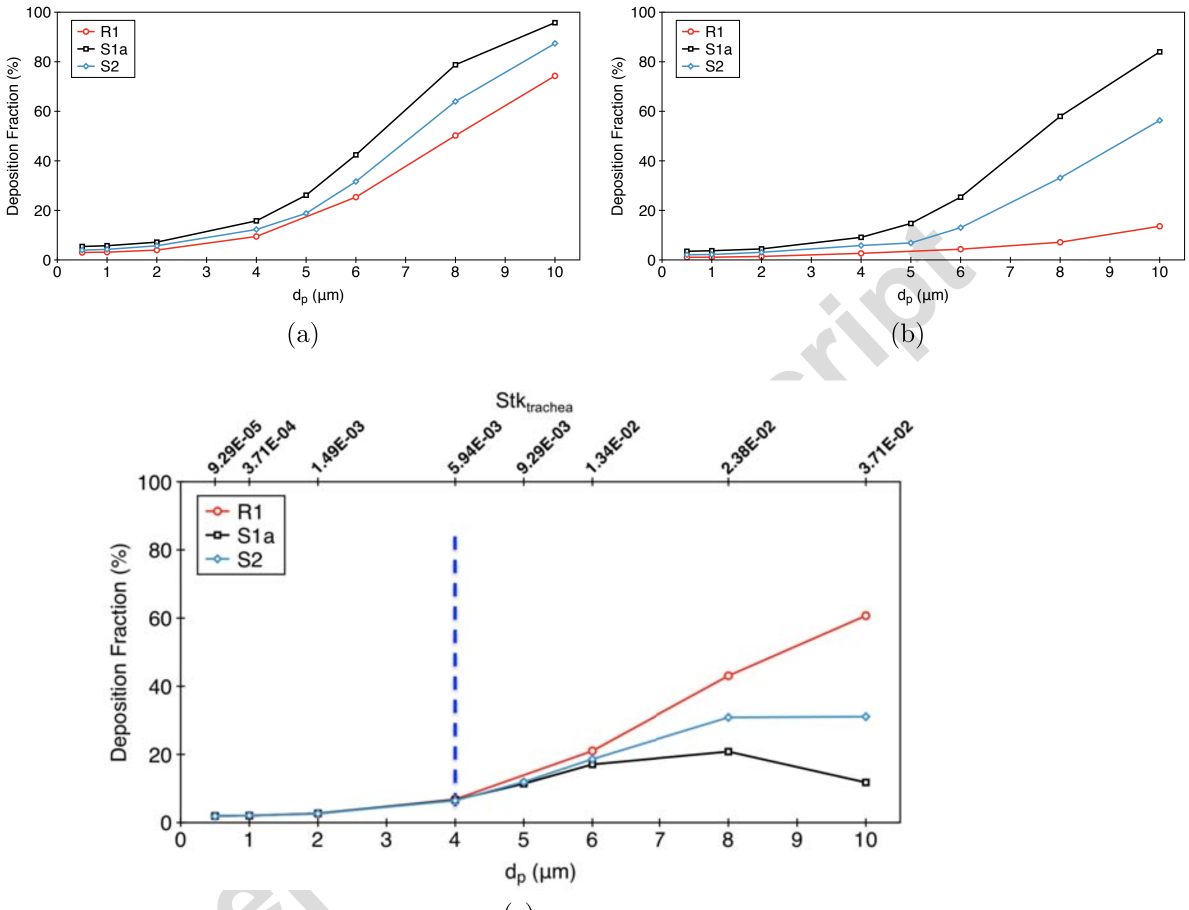

(a)

(b)

(c)

Figure 13: Deposition fractions versus particle size at $Q = 30\,L/min$: (a) overall; (b) mouth and throat; and (c) tracheobronchial. In (c), the Stokes numbers based on tracheal parameters are also displayed.

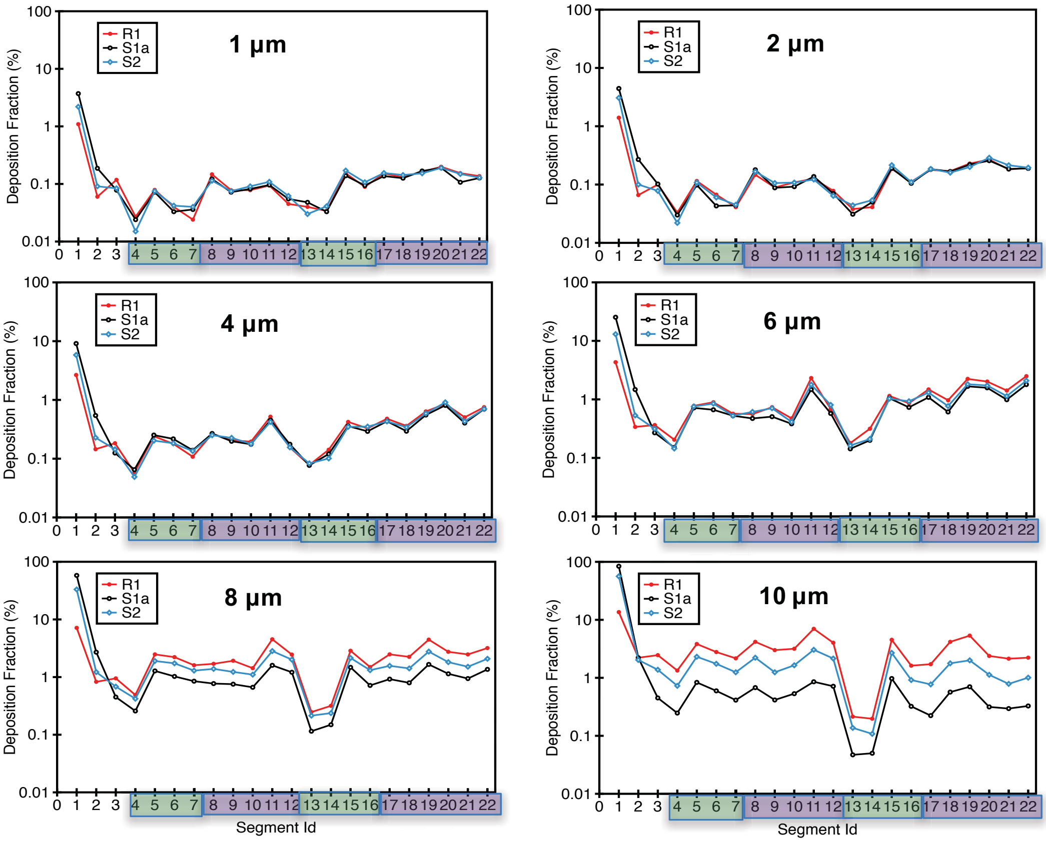

Figure 14: Deposition fractions per segment at $Q = 30\,L/min$ for various particle sizes. The numbering of the segments is shown in fig. 2. The green and purple coloring denotes segments in the left and right lung, respectively. Segment 1 corresponds to the mouth-throat region.

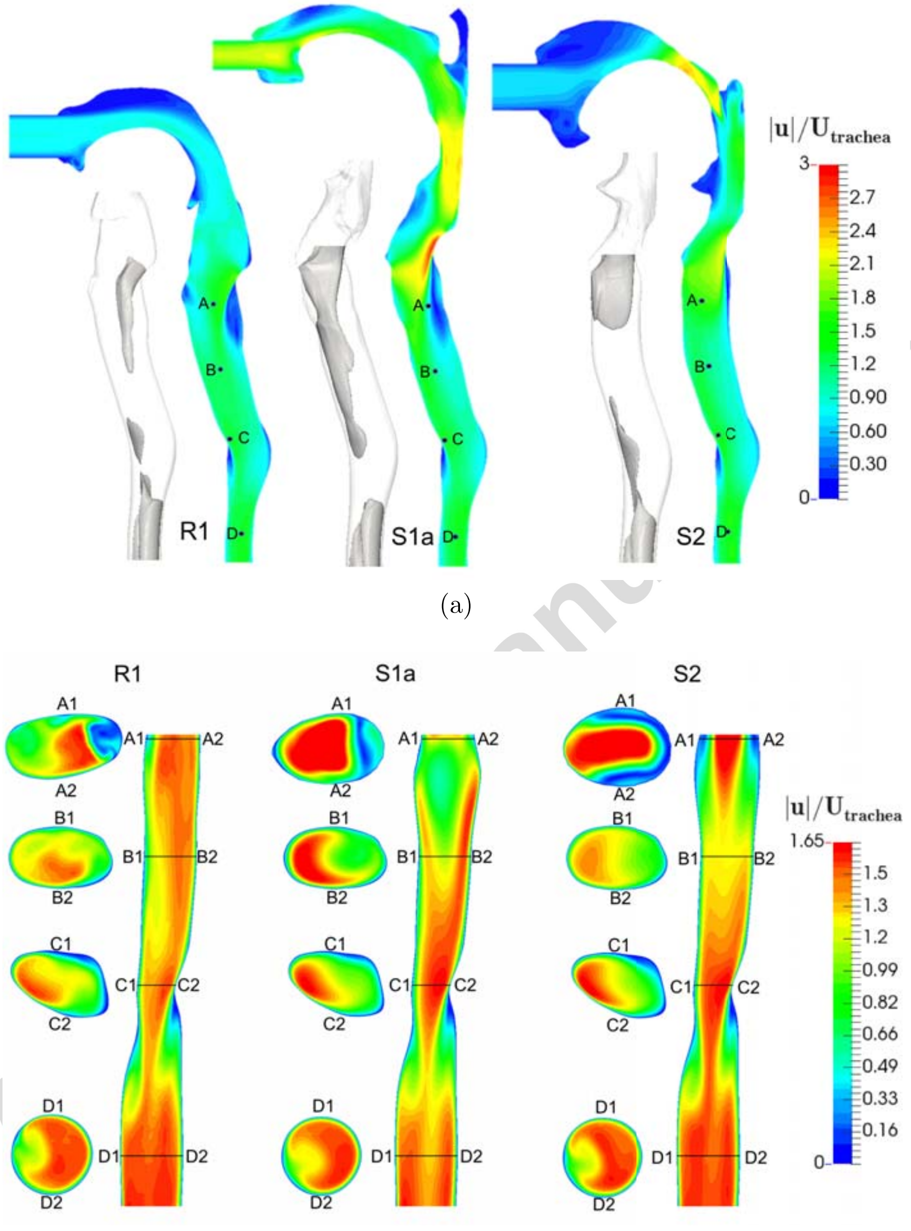

(a)

(b)

Figure 15: Contours of normalized mean velocity magnitude in (a) the mouth-throat region (side view), and (b) the trachea (top and front views) at $Q = 60\,L/min$. In (a) isosurfaces of $|u|/U_{trachea} = 1.35$ are shown.

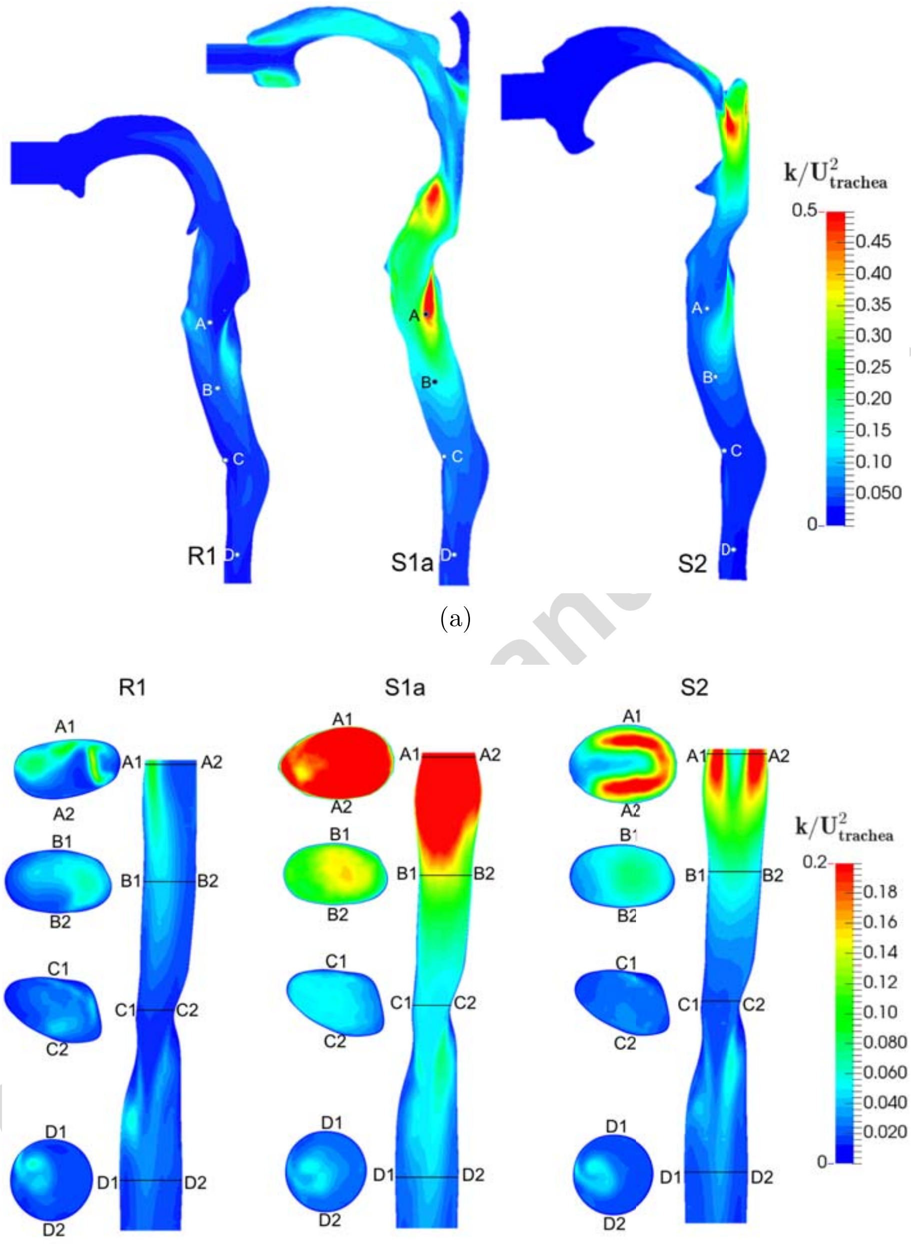

(a)

(b)

Figure 16: Contours of normalized turbulent kinetic energy in (a) the mouth-throat region (side view), and (b) the trachea (top and front views) at $Q = 60\,L/min$.

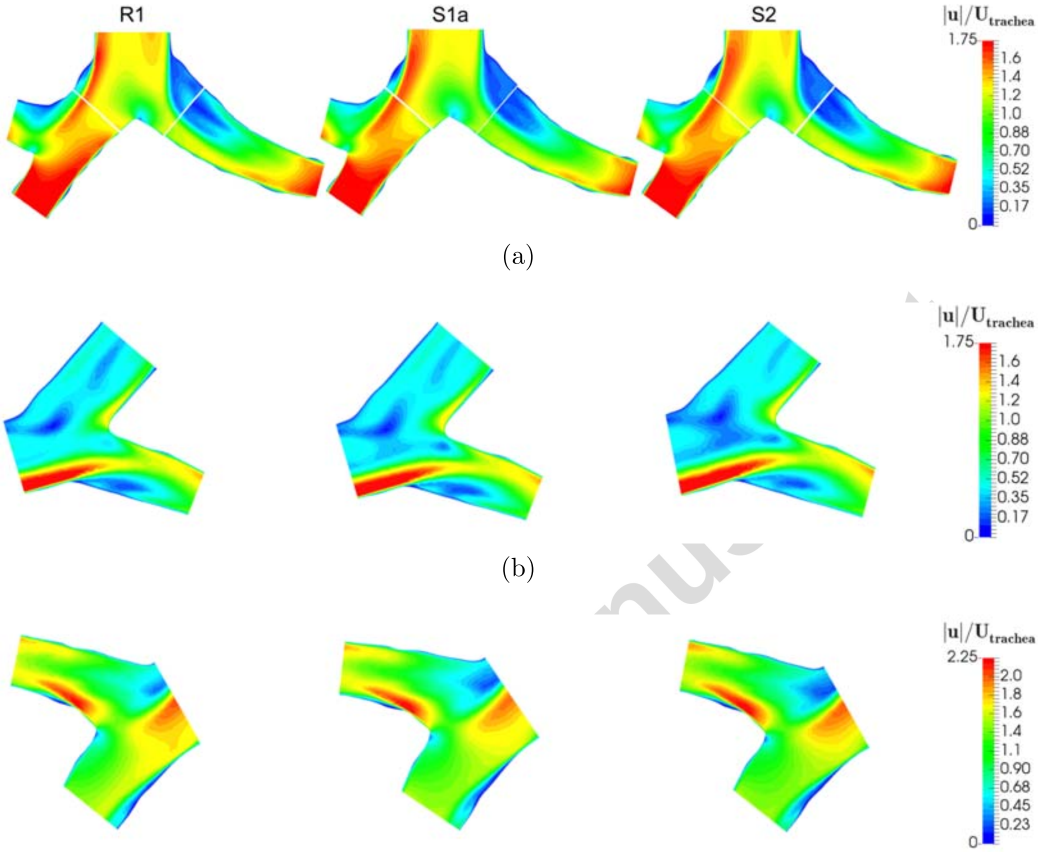

(a)

(b)

(c)

Figure 17: Contours of normalized mean velocity magnitude in the tracheobronchial tree at $Q = 60\,L/min$: (a) first bifurcation and main bronchi; (b) third to fourth generation bifurcation in the left lung; and (c) third to fourth generation bifurcation in the right lung.

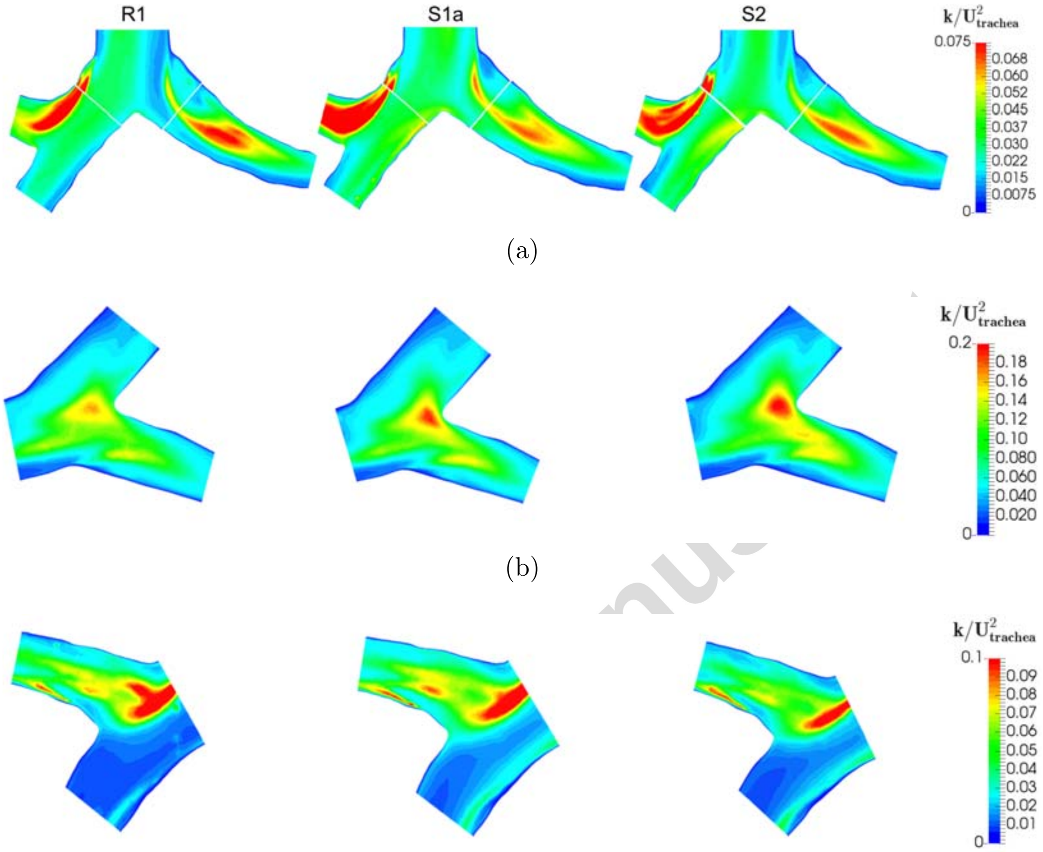

(a)

(b)

(c)

Figure 18: Contours of normalized turbulent kinetic energy in the tracheobronchial tree at $Q = 60\,L/min$: (a) first bifurcation and main bronchi; (b) third to fourth generation bifurcation in the left lung; and (c) third to fourth generation bifurcation in the right lung.

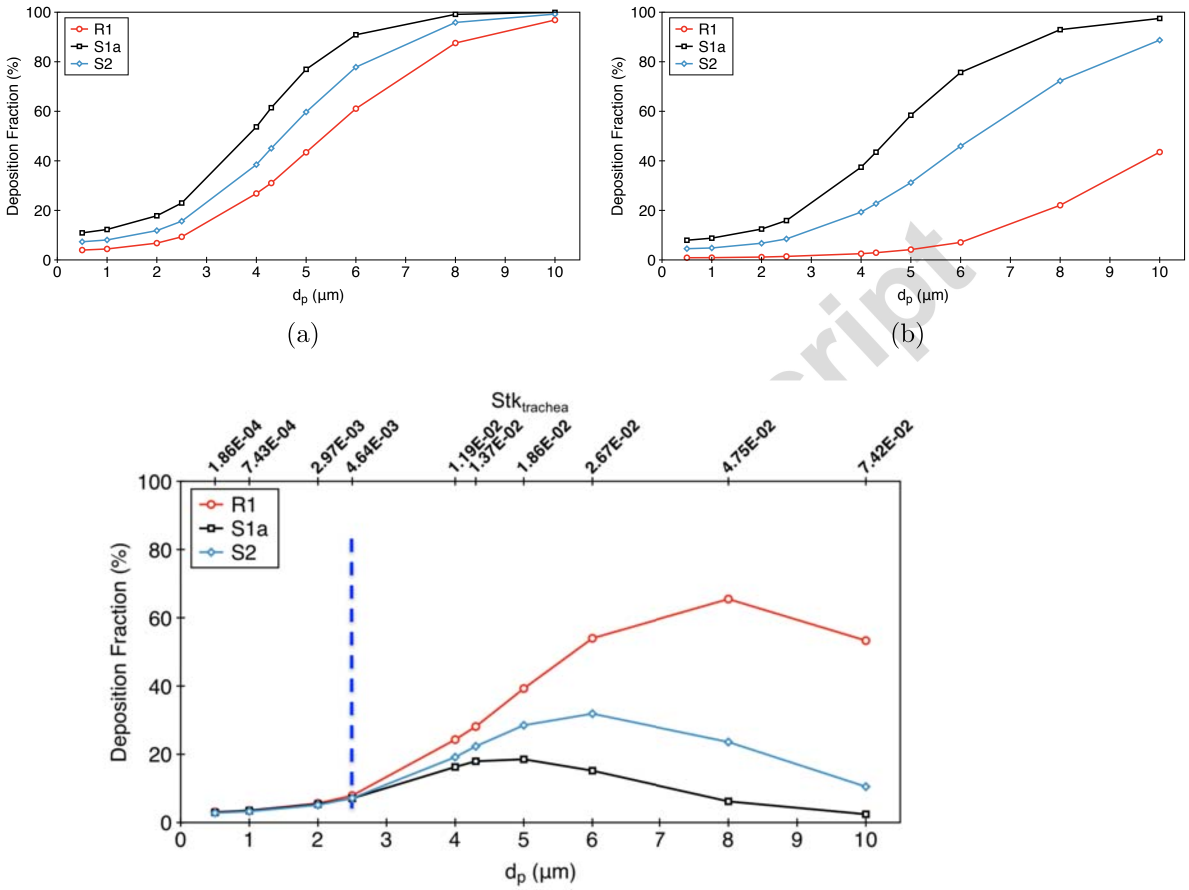

(a)

(b)

(c)

Figure 19: Deposition fractions versus particle size at $Q = 60\,L/min$: (a) overall; (b) mouth and throat; and (c) tracheobronchial. In (c), the Stokes numbers based on tracheal parameters are also displayed.

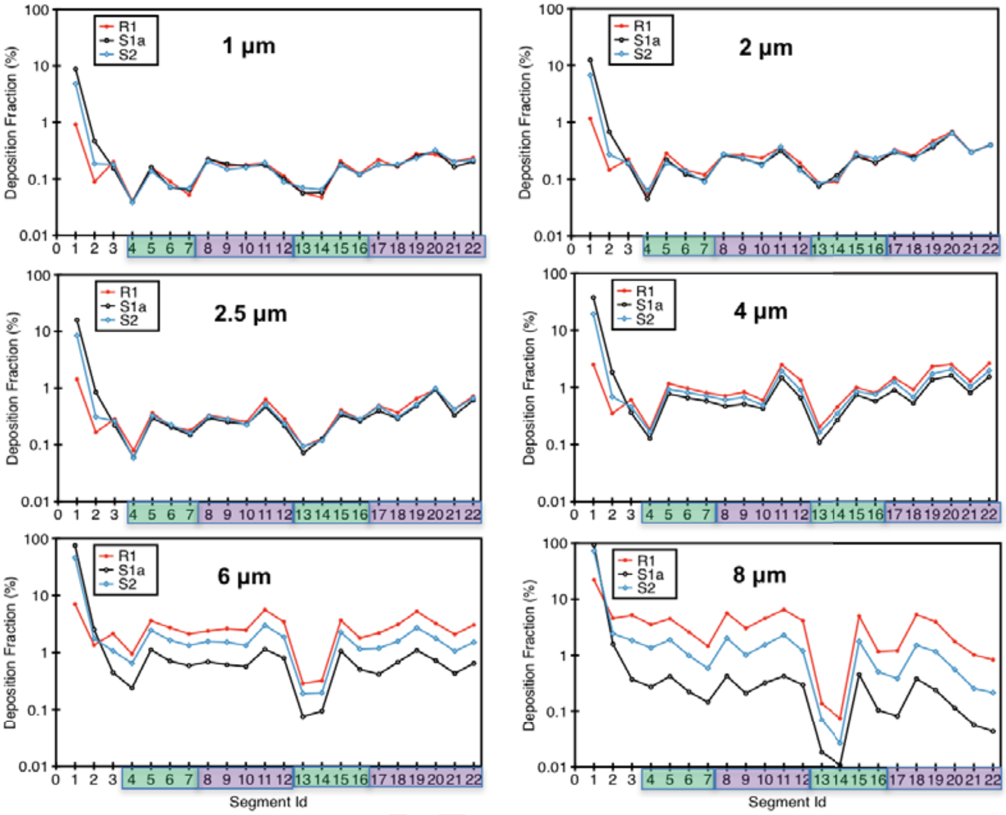

Figure 20: Deposition fractions per segment at $Q = 60\,L/min$ for various particle sizes. The numbering of the segments is shown in fig. 2. The green and purple coloring denotes segments in the left and right lung, respectively. Segment 1 corresponds to the mouth-throat region.

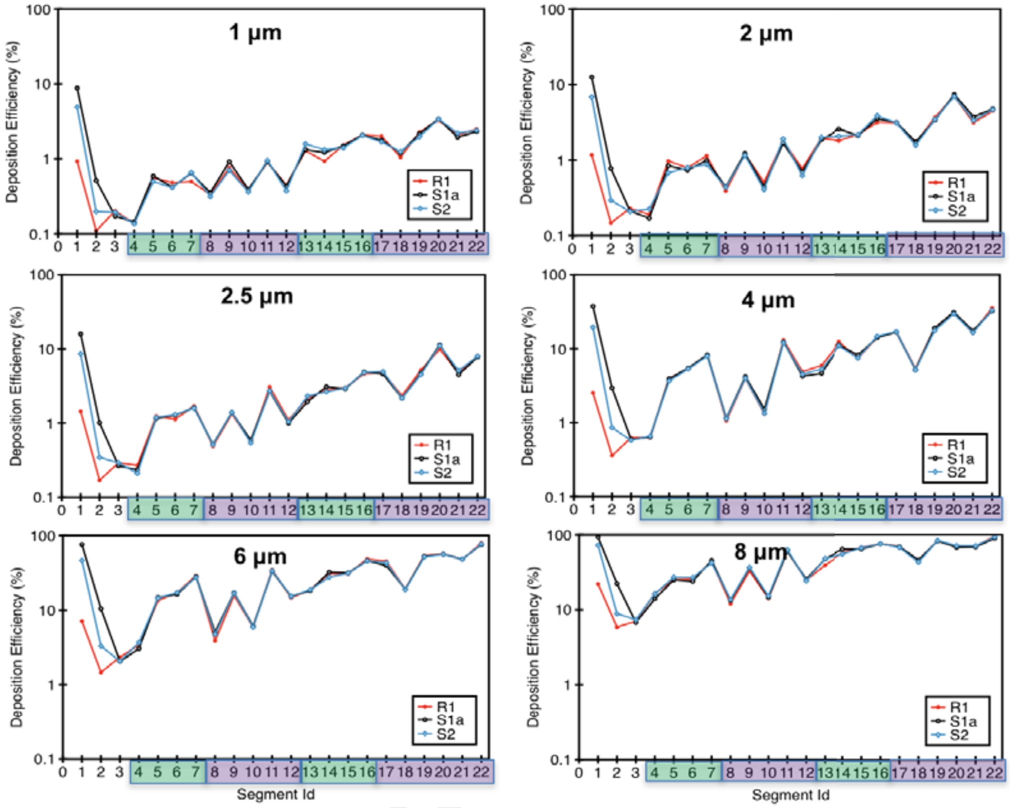

Figure 21: Deposition efficiencies per segment at $Q = 60\,L/min$ for various particle sizes. The numbering of the segments is shown in fig. 2. The green and purple coloring denotes segments in the left and right lung, respectively. Segment 1 corresponds to the mouth-throat region.

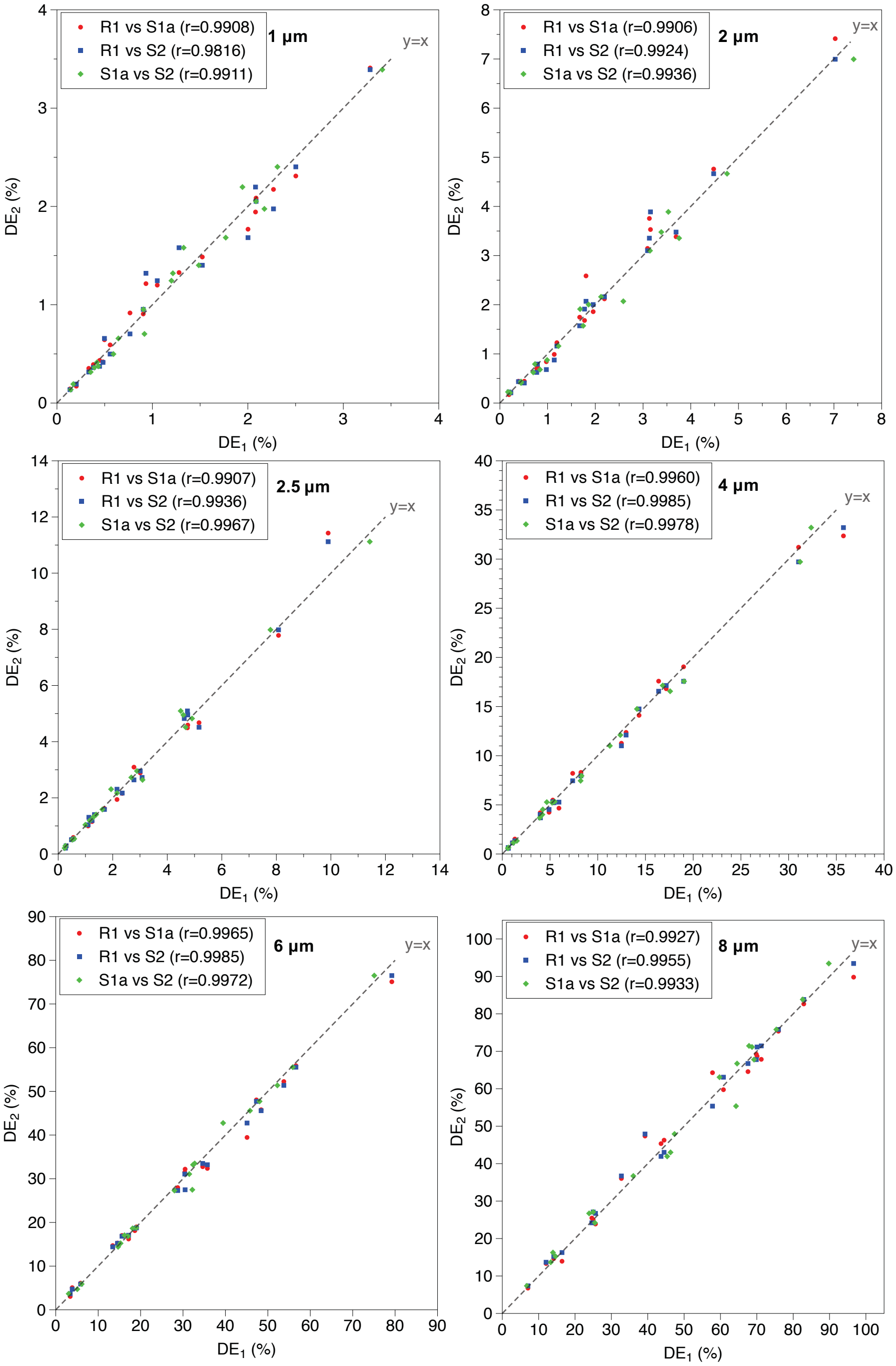

Figure 22: Pairwise scatter plots of segmental deposition efficiencies for various particle sizes at $Q = 60\, L/min$. Pairwise correlation coefficients, r, are also displayed.

List of Tables

Mouth-throat model	R1	S1a	S2
$\mathrm{D}_{\mathrm{inlet}}$ (cm)	2	1.3	2.3
Volume (cm^3)	69.25	51.56	81.73
Length (cm)	15.86	19.1	18.6
$\mathrm{D}_{\mathrm{mean}}$ (cm)	2.36	1.85	2.37
$A_{glottis}/A_{trachea}$	0.716	0.456	0.492

Table 1: Dimensions of the mouth-throat geometries.

Mouth-throat model	R1	S1a	S2
$Q(L/min)$	30 / 60	30 / 60	30 / 60
$\mathrm{U}_{\mathrm{inlet}}$ (m/s)	1.59 / 3.18	3.77 / 7.54	1.2 / 2.4
$\mathrm{U}_{\mathrm{trachea}}$ (m/s)	2.4 / 4.8	2.4 / 4.8	2.4 / 4.8
$\mathrm{R}e_{\mathrm{inlet}}$	1871 / 3742	2883 / 5766	1628 / 3256
$\mathrm{R}e_{\mathrm{trachea}}$	2300 / 5600	2300 / 5600	2300 / 5600

Table 2: Mean velocity and Reynolds number at the inlet and the trachea for the three geometries at the two flowrates examined.

Mesh	1	2	3	4
$\Delta r_{min}(mm)$	0.081	0.065	0.065	0.022
Prism layers	4	4	4	8
λ	1.22	1.22	1.22	1.22
Comp. cells ($\times 10^6$)	7	12	24	42
$V_{cell,avg.}(mm^3)$	0.01	0.0063	0.0032	0.0018
Max y^+	3.27	3.73	3.76	1.48
Avg. y^+	0.88	0.73	0.71	0.24

Table 3: Characteristics of Meshes 1-4 generated for the preliminary tests in the S1a mouth-throat geometry. Δr_{min} is the initial cell height, λ the average expansion ratio of the prism layers and $V_{cell,avg.}$ the average cell volume in the domain.